POLITECNICO
MILANO 1863

SCUOLA DI INGEGNERIA INDUSTRIALE
E DELL'INFORMAZIONE

Scaling Relations for the Geometry of Wire-to-Airfoil Atmospheric Ionic Thrusters

Tesi di Laurea Magistrale in
Aeronautical Engineering - Ingegneria Aeronautica

Author: **Omar Kahol**

Student ID: 962740
Advisor: Prof. Marco Belan
Academic Year: 2022-23

Abstract

This work presents a multiparameter experimental investigation on the effects of geometrical parameters on the performance of corona thrusters. A scaling model is presented in order to define physically consistent reference values and dimensionless coefficients that describe the main performance indicators. Airfoil collectors of different thickness and chord are tested in a parallel array configuration at different spacings, gaps and voltages. Direct thrust and electrical measurements are performed and used to determine the dimensionless coefficients. The results identify scaling relations and indicate that collectors with short chord and adequate thickness maximize, within the investigated parameter space, the performance parameters.

Keywords: EHD propulsion, DC Corona Discharge, Ionic Emitters configuration, Atmospheric Ionic Thruster. Thruster.

Abstract in lingua italiana

Questo lavoro presenta un'indagine sperimentale multiparametrica sugli effetti dei parametri geometrici sulle prestazioni dei propulsori a corona. Viene presentato un modello di scaling per definire valori di riferimento fisicamente consistenti e coefficienti adimensionali che descrivono i principali indicatori di prestazione. Profili di diverso spessore e corda vengono testati in una configurazione multiprofilo a diversi spaziature, gap e tensioni. Sono state effettuate misure dirette di spinta ed elettriche per determinare i coefficienti adimensionali. I risultati evidenziano relazioni di scaling e indicano che i collettori con corda corta e spessore adeguato massimizzano, nello spazio dei parametri indagati, i parametri di prestazione.

Parole chiave: Propulsione EHD, Scarica a corona, Propulsore ionico atmosferico, elettrodi corona.

Contents

1 | Introduction

Since the beginning of the aviation era, aeroplanes have always been powered by moving parts propulsive systems such as propellers and turbine engines with consequent high consumption of fossil fuels. The new trend of scientific and technological development is oriented towards the reduction of carbon emissions in favour of renewable energies. In the aerospace sector, electrical propulsion techniques are regarded as a promising and valid alternative to fossil fuel ones [3, 4]. Among all, ionic thrusters have been already widely and successfully used for space applications [5, 10, 23]. Although nowadays they are still not employed in atmospheric flight applications, in the last years the interest for Electrohydrodynamic (EHD) propulsion in this field is rapidly growing as an alternative to conventional engines. Ionic propulsion would provide several advantages for atmospheric flight such as the high efficiency in terms of thrust-to-power ratio, absence of moving parts, low maintenance, low noise emissions and the high sustainability of this kind of propulsive system deriving from electric power consumption [7, 11, 17, 24, 25, 30, 31].

1.1. EHD Thrusters

An EHD thruster, in its simplest version, is composed by two electrodes separated by a distance called gap. The ion emitter is typically a metallic wire of radius smaller than 100 µm, while the ion collector is a larger electrode with a conductive surface that can assume different shapes. These simple devices exploit the corona effect to create an ionic wind able to generate a net thrust. A strong asymmetric electric field between the electrodes is imposed applying a sufficiently high voltage difference with a suitable power supply. The electric field ionizes the gas surrounding the emitter, in turn creating a corona discharge where the drifting motion of the ions transfers momentum to the neutral molecules.

Starting from these basic elements, there was an evolution along the years that has led to different configurations. The scientific progress has advanced from simple geometries with cylindrical collectors to more sophisticated ones with airfoil collectors, with the objective of optimizing the performance.

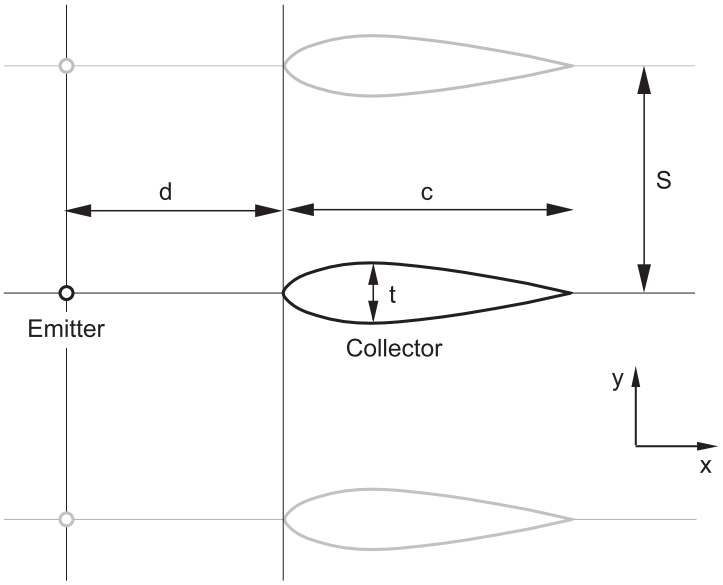

Figure 1.1: Geometry and parameters of an EHD thruster in a multiple units wire-to-airfoil configuration

As depicted in Fig. 1.1, in each unit the emitter and the collector are separated by a gap d. The main geometric parameters for the collector are the chord c and the thickness t. This configuration can be replicated along the y direction, with spacing S, to obtain a multiple units configuration. The space between adjacent units is also indicated as *thruster cell*.

1.2. Physics of the ionization process in gases

1.2.1. Breakdown in uniform fields

The foundational study of electrical breakdown in gases was conducted by Townsend [28]. This research involved measuring the current generated by a capacitor with two parallel plates, under varying pressures, voltages, and gaps. The qualitative behavior of the current in relation to the applied voltage is depicted in Figure 1.2.

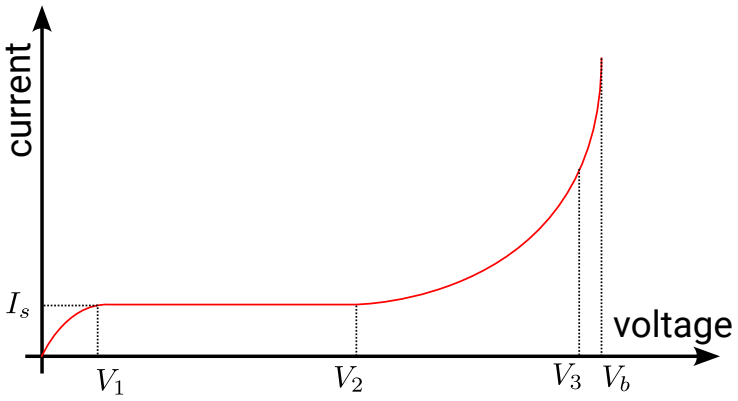

Figure 1.2: Current-Voltage curve for a gaseous discharge in a parallel plates capacitor

Townsend's findings indicated that as soon as a voltage is applied, a small current can be recorded, which is known as the "saturation current" or "background current". This current is a result of natural breakdown caused by random thermal and photo-ionization effects, and is usually very small, ranging from pico- to nano-amperes. The saturation current remains relatively constant across a wide range of voltages. However, once the voltage surpasses a certain threshold, V_2, an exponential behavior is observed. This behavior is caused by an avalanche mechanism, as depicted in Figure 1.3. Electrons generated at the cathode are accelerated by the electric field of the capacitor, $E = \frac{V}{d}$, and the energy transferred through collisions with neutral atoms has the capability to ionize the gas, leading to an exponential increase in the current.

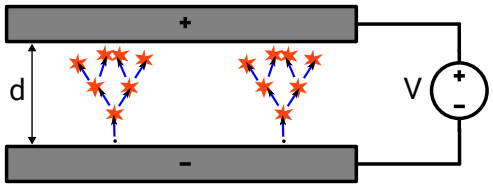

Figure 1.3: Depiction of the avalanche mechanism

The mathematical representation of the avalanche breakdown can be formulated using the following equation [19]:

$$I = I_s \left(\frac{\alpha}{\alpha - \eta} e^{(\alpha - \eta)d} - \frac{\eta}{\alpha - \eta} \right) \tag{1.1}$$

where I is the current measured at the anode, I_s is the saturation current produced at the cathode, d is the distance between the cathode and the anode, and α is the so-called *Townsend first coefficient*. This coefficient is defined such that the exponential $e^{\alpha d}$

represents the number of electrons produced by a single electron leaving the cathode and undergoing an avalanche process.

In other words, α characterizes the rate at which the number of ionized particles increases during the breakdown process. It is a measure of the ionization efficiency of the gas and is dependent on several factors, including the pressure, the gap distance, and the nature of the gas. The number of electrons produced by the avalanche process is affected by electron losses due to reattachment and attachment, which is accounted for by the coefficient η.

Kinetic theory provides a first order functional form of the first ionization coefficient as a function of the pressure, P, electric field E and temperature T

$$\alpha = P\mathcal{A}\, e^{\frac{\mathcal{B}P}{E}} \tag{1.2}$$

Table 1.1: Ionization constants at 300 K

Symbol	Value	Unit
$\mathcal{A}$	9.29	$\mathrm{cm^{-1}torr^{-1}}$
$\mathcal{B}$	295.18	$\mathrm{cm^{-1}torr^{-1}}$

It is crucial to note that the avalanche breakdown regime is not self-sustaining. The avalanche process relies on the generation of electrons at the cathode by external factors, such as thermal and photo-ionization. However, at high voltages, after V_3, the current deviates from the exponential behavior due to the activation of secondary ionization mechanisms. Positive ions impacting the cathode surface can generate new ion-electron pairs, and sufficiently energetic electrons can release photons that ionize neutral gas molecules (particularly important in corona discharges). Townsend law can be modified with

$$I = I_s \frac{\left(\frac{\alpha}{\alpha-\eta} e^{(\alpha-\eta)d} - \frac{\eta}{\alpha-\eta}\right)}{1-\gamma\left(e^{(\alpha-\eta)d}-1\right)} \tag{1.3}$$

The secondary emission effects are accounted for by the introduction of the second ionization coefficient, γ, which changes the denominator of the cathode current. For air at standard conditions, this coefficient has a value of $\gamma = 0.01$. It is important to note that as the voltage is increased, the denominator in the equation approaches zero, at which

point the avalanche process becomes self-sustaining, resulting in complete breakdown by arcs or sparks. This is known as the Townsend criterion and is the voltage at which it occurs is computed by means of Paschen's law

$$V_b = \frac{\mathcal{B}\ Pd}{\ln\left(\mathcal{A}\ \mathrm{Pd}\right) - \ln\left(\ln\left(1 + \frac{1}{\gamma}\right)\right)} \tag{1.4}$$

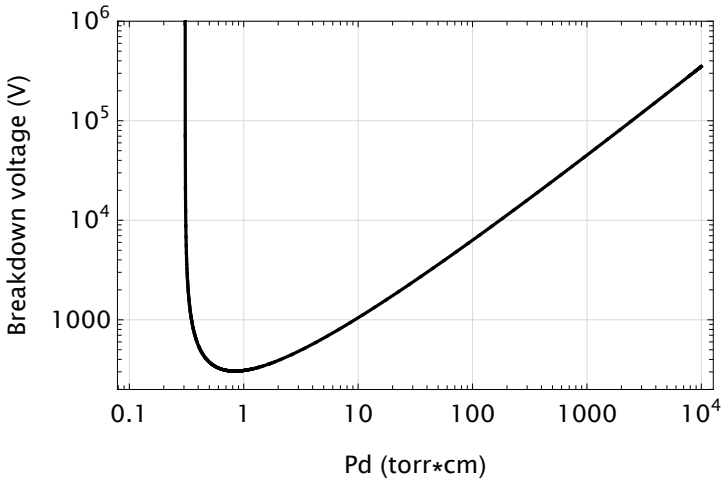

Figure 1.4: Breakdown voltage in air

It is crucial to emphasize that this mathematical treatment of the avalanche breakdown is only valid when the impact of space charges is negligible. If this is not the case, the presence of space charges can cause a distortion of the local electric field, leading to a different type of electrical breakdown known as streamer breakdown. In this scenario, the electric field is distorted, and the breakdown dynamics become much more complex. The breakdown is characterized by the propagation of streamers, which are luminous filaments that travel through the gas, ionizing it and creating channels for the flow of current.

1.2.2. Breakdown in non-uniform fields

In the presence of a non-uniform electric field, electrical breakdown can result in a diverse range of stable discharges that are both luminous and audible. Unlike the case of a uniform electric field, where breakdown usually occurs abruptly in the form of sparks or arcs, a non-uniform distribution of electric field magnitude can lead to a more complex and varied display of discharge phenomena.

The Townsend breakdown criteria cannot be used here because the mechanism depends

on secondary effects at the cathode, as described by γ. The electric field strength at the cathode is typically low due to its large curvature radius. In this case, it is possible to have a partial breakdown, most commonly known as corona, in which ionization occurs only in the vicinity of the anode in a region which is called the *ionization region*.

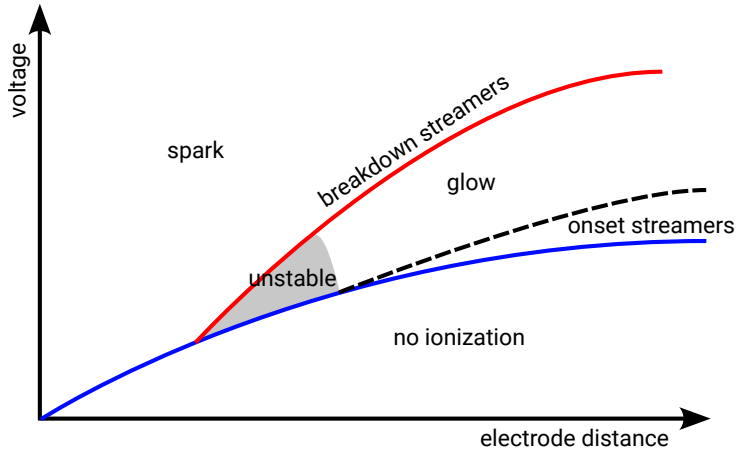

Figure 1.5: Qualitative representation of the different regimes for a pin-plate configuration [19]

Fig.1.5 shows the different regimes for a pin-plate configuration as a function of the pin voltage (positive) and the electrode spacing. It is possible to observe that, at low gaps, Townsend mechanism applies and there is a sudden transition to spark and arc breakdown. At sufficiently high gaps, Townsend mechanism loses its validity and the breakdown is anticipated by two different regimes. As the voltage is increased, space charge density near the anode becomes high enough to distort the local electric field and give rise to streamer discharge. These luminous filaments are ionized channels of different lengths and frequencies. The appearance of these streamers is called *inception* and the voltage value at which they appear can be computed using a modified version of the Townsend mechanism [8]

$$\int_0^x e^{(\alpha-\eta)x}\ \mathrm{dx} = \mathrm{N_{cr}} \tag{1.5}$$

In Eq.1.5, N_{cr} is the critical number density of space charges necessary to develop a streamer, $\mathrm{lnN_{cr}}$ is 18-20 for positive corona or 6-8 for negative corona [8]. It is however possible to refer this criterion to a required electric field, E_i, necessary for corona inception. The empirical calculations of this field (valid only for simple geometries) are due to Peek [27]

$$E_i = E_b\delta(1 + \frac{k_1}{\sqrt{\delta r_e}}) \tag{1.6}$$

The field E_b is the magnitude of the breakdown field of the gas, δ is the is the gas number density normalized to the gas density at ambient conditions, r_e is the electrode radius and k_1 is an empirical dimensional constant. It has been observed [15] that the value of the inception field remains constant during the onset and the glow regime. The value of the inception field can be related to a voltage, which is called *inception voltage* and is defined as the voltage difference necessary to trigger the breakdown in the ionization region. This parameter is of paramount importance for the performance of an EHD thruster.

When the voltage is further increased, the onset streamers become more frequent until they stop and the discharge becomes self sustained due to secondary effects such as photo-ionization. This regime is called *glow*.

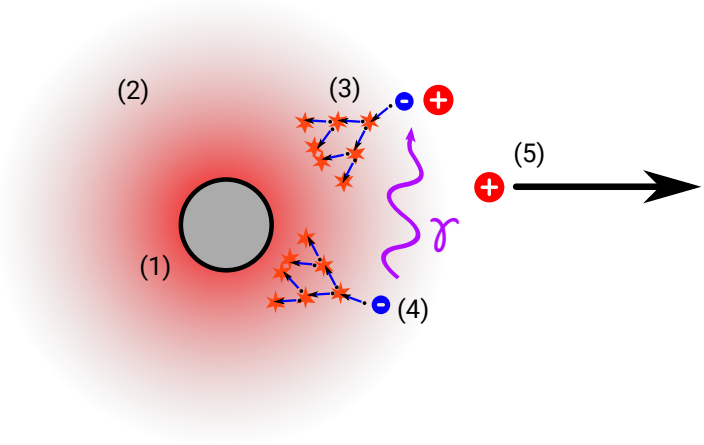

Figure 1.6: Qualitative representation of the ionization region around a positively charged emitter wire.

Fig.1.6 shows the ionization region (2) near a small radius emitter (1). Highly energetic electrons (4) emit photons that are capable of ionizing neutral molecules. The electrons undergo the classical Townsend avalanche mechanism (3) while positive ions (5) migrate towards the cathode. Far away from the anode, the electric field strength is not sufficient enough to favour ionization and the positive ions undergo drift-diffusion processes exchanging their kinetic energy with the neutral gas. The detailed mechanism for the generation of an airflow, and therefore thrust, is provided in Chapter 2 along with the development of a dimensionless model and theoretical estimations.

A further increase in the voltage can give rise to more streamers which ultimately lead to a complete breakdown via arcs or sparks.

1.3. State of the art of EHD thrusters

The behavior of an EHD thruster is evaluated using two primary performance parameters: the thrust-to-power ratio, T/P, and the thrust density, T/A. In Chapter 2, a self-consistent dimensionless model will be developed alongside theoretical predictions to explain the behavior of these parameters with respect to both physical and geometric conditions. However, it is worthwhile to note that these quantities scale as follows:

$$\begin{cases} \dfrac{T}{P} = \dfrac{\mu_q d}{V_a} C_{TP} \\ \dfrac{T}{A} = \epsilon_0 \dfrac{V_a^2}{d^2} C_{TA} \end{cases} \tag{1.7}$$

If we assume that both dimensionless coefficients have an order of 1, the two primary performance indicators exhibit opposite behavior as the ratio of applied voltage to gap distance, V_a/d, increases. A low value of this parameter enhances the thrust-to-power ratio, whereas a high value of the parameter enhances the thrust density. As a result, the power density, represented by the parameter $\frac{P}{A}$, which measures the power required per unit area, increases with the third power of the voltage-to-gap ratio.

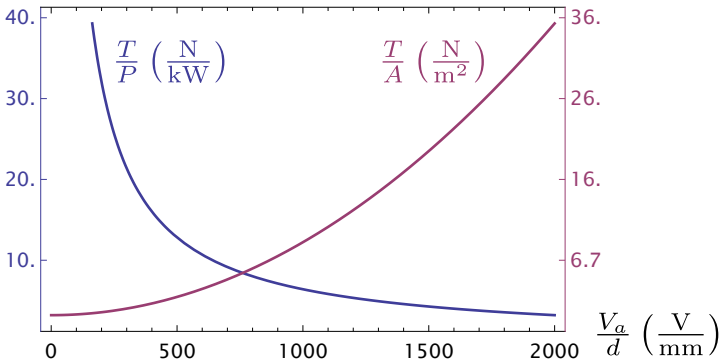

Figure 1.7: Reference values for the thrust to power and thrust density of an EHD thruster

As shown in Fig. 1.7, a theoretical ionic thruster is capable of achieving a higher thrust-to-power ratio than conventional jet propulsion, with values of up to $2\,\frac{\mathrm{N}}{\mathrm{kW}}$. However, the thrust density is orders of magnitude smaller and power requirements don't scale well with the thruster's frontal area.

For optimal design, it is imperative to ensure high efficiency and low weight, and these results suggest that there is still ample room for improvement in both the geometric parameters and the practical application of this technology. Nevertheless, the field of EHD propulsion has seen several remarkable outcomes in recent years. This section highlights some of the most intriguing research, including the EHD propulsion aeroplane, Ionocraft, and Polimi experimental thrusters.

1.3.1. MIT Aeroplane

In 2018, a remarkable achievement was made by a team from MIT [32], who successfully propelled a heavier-than-air airplane using corona discharge technology during level flight. This breakthrough was the culmination of years of extensive research and development in this field, which were spearheaded by [9, 22]. Through their studies, they were able to measure and analyze the variations of thrust density and thrust to power for different gaps and emitter radii, which laid the foundation for the eventual success of the project.

Figure 1.8: Picture of the MIT EHD aeroplane [32]

The airplane, named the EHD airplane, is depicted in Figure 1.8 and was designed with an on-board power and energy supply, allowing it to perform short, self-sustained flights within a controlled laboratory environment. The key component of the aircraft was a dual stage thruster, which utilized an array of 4 NACA0010 airfoils as collectors and 200 µm stainless steel wire as emitters held at a distance of 60 mm. The half wing span is 1 m. A qualitative representation of the dual stage thruster is given in Figure 1.9.

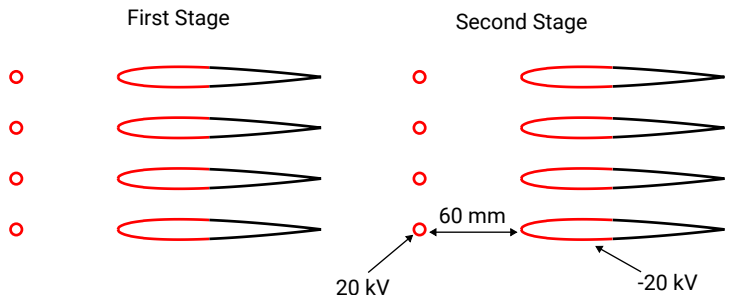

Figure 1.9: Qualitative depiction of the MIT airplaine dual stage thruster [32]

The performance indicators for the airplane are reported in the following table.

Table 1.2: Performance parameters of the MIT EHD airplane

Name	Value	SI unit
Thrust Density	3.56	N/m^2
Thrust to Power	5.16	N/kW
Velocity	5	m/s
Distance	50	m

The detailed geometry was found by means of an optimization procedure which had the total wingspan as objective.

1.3.2. Ionocraft

The lifter by Khomich and Rebrov [16] is another example of a thruster that has successfully achieved flight. Unlike conventional aircraft, this particular thruster takes off vertically and is able to lift its own weight due to its impressive power-to-weight ratio. This exceptional ratio was achieved through the use of a lightweight design and a wireless power transmission system, which eliminates the need for on-board batteries. Figure 1.10 shows a picture of the ionocraft.

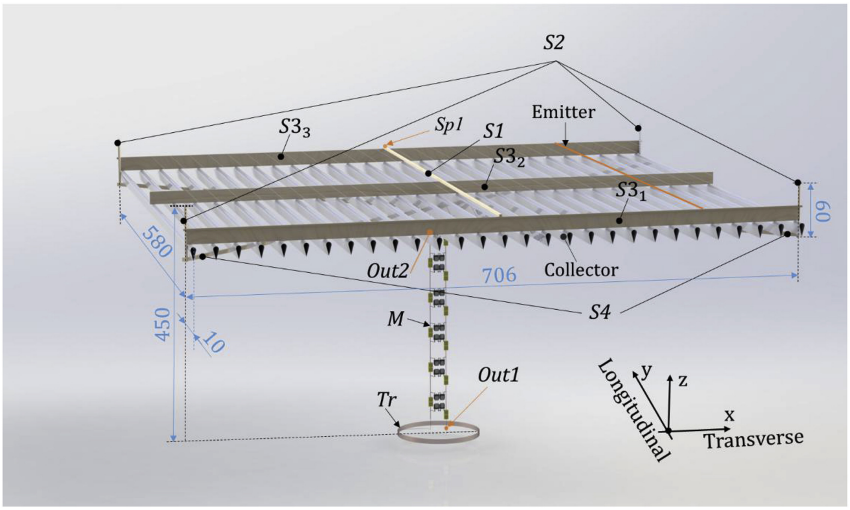

Figure 1.10: Picture of the ionocraft [16]

The lifter consists of an array of evenly spaced wires acting as emitters, positioned in front of drop-shaped airfoils serving as collectors, arranged in an offset manner. This realizes an array of 28 cells with a total span of 580 mm. The particular geometry is shown in 1.11 and Table 1.3 reports the numerical values of such parameters.

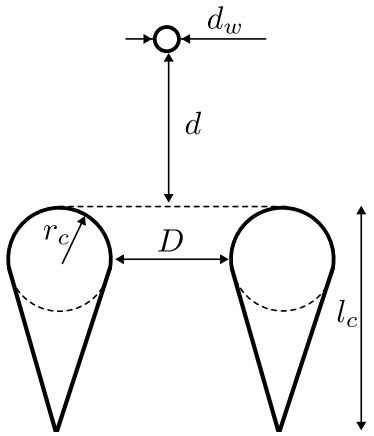

Figure 1.11: Geometric parameters of the Ionocraft

Table 1.3: Geometric parameters of the Ionocraft

Name	Value	Description
r_c	3 mm	Collector Curvature Radius
l_c	17 mm	Collector Length
d_w	80 µm	Emitter Diameter
d	8.2 mm	Gap
D	19 mm	Collector Spacing

Interestingly enough, the collectors have a much smaller chord with respect to the MIT airplane (which used 100 mm NACA0010 airfoils). The corona discharge is powered by a voltage that ranges from 11 kV to 13 kV which correspond, respectively, to the voltage required to achieve lift and the breakdown voltage. The performance parameters for the thruster are reported in the following table:

Table 1.4: Performance parameters of the MIT EHD airplane

Name	Value	SI unit
Thrust Density	3.77	N/m^2
Thrust to Power	5.15	N/kW

1.3.3. Rotary Ionic Engine

Another noteworthy application of ionic engine technology is the rotary ionic engine by Chirita et al. [7, 11–13]. In this case, propells blades have metallic pins attached to their ends which play the role of emitters. The collector is a grounded cylindrical box that encapsulates the rotor.

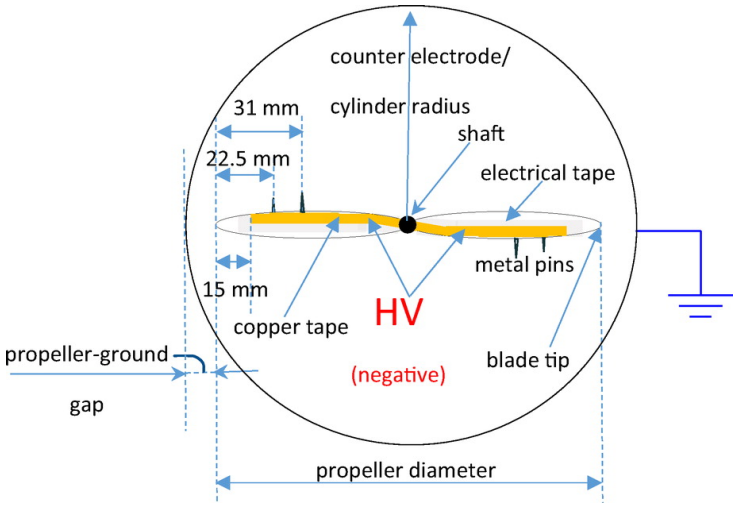

Figure 1.12: Depiction of the geometric of the ionic propeller by [7]

The propeller system, shown in Figure 1.12, uses the corona effect to generate a torque on the blades which results in the generation of a net thrust force. The system is powered by a 35 kV potential. Several studies were performed to improve the resulting RPM and thrust, leading to innovations such as the use of contra-rotating propellers [7] and toroidal grounded electrodes instead of cylindrical ones [12]. The system can reach 2500 RPM and generate 800 mN of thrust.

1.3.4. PoliMi Thrusters

At the Aerospace Department of Politecnico di Milano, two experimental setups are present which allows for in depth investigations of the physics of ionic engines.

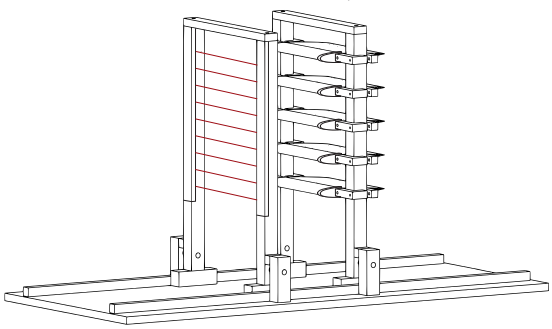

(a) Velocity Measurement Setup

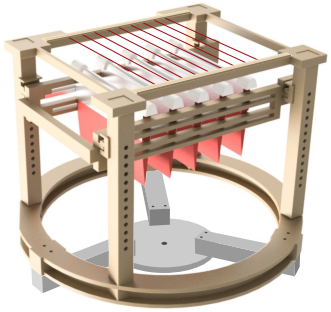

(b) Direct Thruster Measurement Setup

Figure 1.13: Detail of the two experimental setups at the DAER

The two setups, shown in Figure 1.13, consists of a setup that, by means of Pitot or hot

wires probes, allows to investigate the airflow generated by the ionic wind. This setup has been used in 2021 [1] to find the optimal airfoil thickness for airfoils with a chord of 100 mm and in 2022 to investigate the airflow generated by different anodes geometry. In the same year [2], a direct thrust measurement setup was also introduced in order to validate and improve previous models which were able to compute the thrust given a particular airflow distribution relying on a set of assumptions. The latter consists of support structure, on which the thruster is mounted, and 3 load cells to measure the forces.

This setup was also used to investigate the effect of increasing the anodic density in the performance parameters.

1.4. Research Parameters

The primary design variable in this work is the shape of the collectors, identifying the thickness and the chord as the main parameters which are used to generate a corresponding NACA 4-digit airfoil.

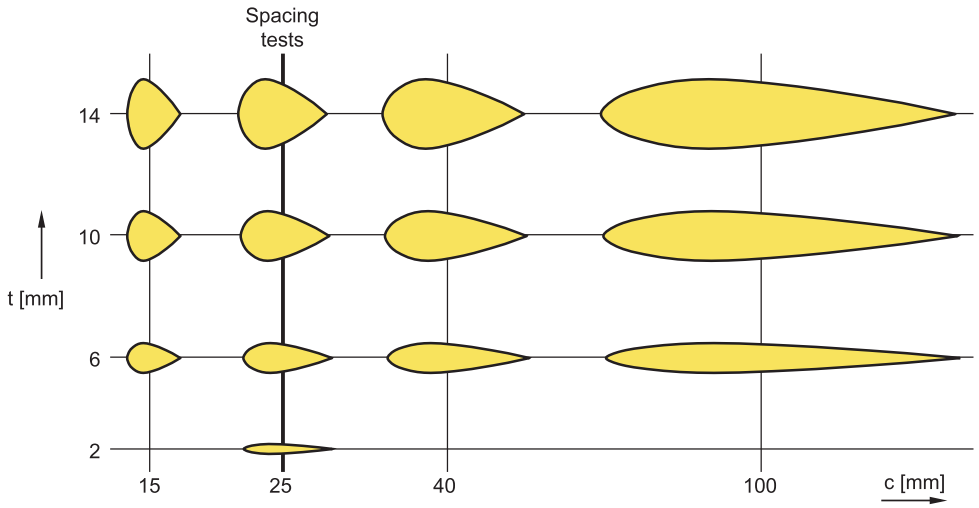

Figure 1.14: Parameter space of airfoils collectors

Fig. 1.14 shows the studied airfoil shapes. The investigated chords are 15, 25, 40 and 100 mm. Each chord family presents airfoils with variable thickness of 6, 10 and 14 mm. A further airfoil with chord 25 mm and thickness 2 mm was introduced during the tests to corroborate the experimental trends. Each configuration will be indicated using CxxTyySzz, where xx indicates the chord in mm, yy the thickness in mm and zz the spacing between units in mm.

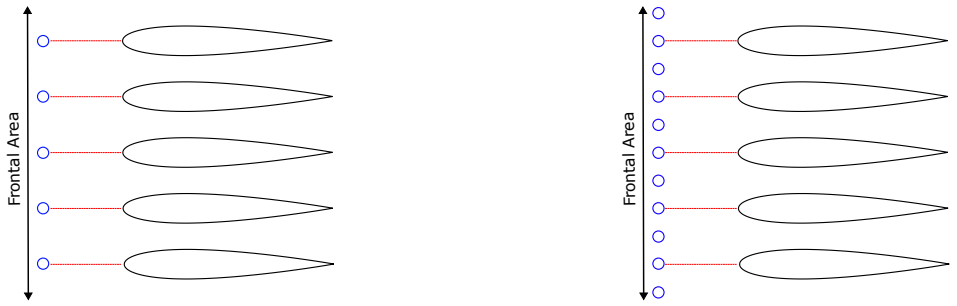

(a) Single Emitter (b) Double Emitter

Figure 1.15: Periodic single and double emitter configurations (geometrical parameters are not to scale)

The general criteria for defining this space are exposed in what follows: airfoils with very long chords are not efficient since they introduce a large amount of parasitic drag due to wall stress. Thus, there is no use in extending the space towards the right side since long airfoils are not an efficient solution for the design of an EHD thruster. Decreasing the chord while keeping the thickness constant would, on the one hand, keep a similar discharge section and consequently a similar electrical thrust; on the other hand, the t/c shape parameter would increase leading to bluff shapes and worsening the aerodynamic performance. Also an increase of thickness keeping the same chord leads to bluff bodies. Consequently, extensions towards the top and left of the parameter space are not viable either. This indicates that a local optimum could be found in the bottom zone of the parameter space, particularly on the left side. However, this region is bounded by some technical limits, since thin and short airfoils may create structural and manufacturing issues. First, these shapes have a lower stiffness compared to thicker airfoils and may introduce misalignments in the electric and motion fields. Secondly, manufacturing such electrodes may lead to several problems depending on the technology, such as the accuracy of 3D prototyping and milling or the preparation of composite structures (for the present work, the limiting factor is presumably the spatial accuracy of the 3D printer).

The dependence of the performance indicators on the gap d is of uttermost importance since the scaling introduced in §2 uses that dimension as a reference for all the other lengths. For this reason, specific tests are devoted to explore the dependence on the gap value. Other tests introduce the voltage variation, since the electric field scale is set by V_a and d. Further tests are introduced in order to study the dependence on the spacing S, a topic already considered on a smaller parameter space in [1].

Moreover, additional experiments are performed by exploring the differences between the

single emitter (SE) and double emitter (DE) configuration shown in Figure 1.15, since in a previous work [2] the double emitter system was shown to have a beneficial effect both on the thrust density and on the thrust to power ratio in a periodic configuration.

The chances of varying c, t, d, V_a, S potentially give rise to an enormous number of combinations, for which it is necessary to establish an investigation criterion, keeping the laboratory time within reasonable limits. In what follows, the parameters are varied separately starting from a standard configuration based on previous investigations, namely:

$$\text{gap } d = 20 \text{ mm; voltage } V_a = 20 \text{ kV; spacing } S = 35 \text{ mm; single emitter.} \tag{1.8}$$

In particular, an initial evaluation is performed for all airfoils in Fig. 1.14 with this standard configuration. Then, a subspace with chord 25 mm (thick line in Fig. 1.14) is selected for further tests, including the spacing dependence in both single and double emitter configuration. Afterwards, the C25T6 airfoil is selected for a study of the gap and voltage dependence.

2 | Drift Region Scaling

In this chapter the governing equations for EHD propulsion are derived starting from first principles. The derivation will highlight how the relevant dimensional quantities interact and will clearly show the mechanism behind the generation of the EHD force.

2.1. Governing Equations

In the drift region, chemistry and ionization, are not relevant therefore it is possible to treat the ions and neutral gas as two different ideal mixtures. The conservation of momentum for the ions and neutral gas, respectively, reads [6]

$$m_q n_q(\frac{\partial \mathbf{v}}{\partial t} + \mathbf{v}\cdot\nabla\mathbf{v}) = -\nabla P_q + \nabla\cdot\sigma_q^{visc} + qn_q\mathbf{E} - m_q n_q \nu^{coll}(\mathbf{v}-\mathbf{u}) \tag{2.1}$$

$$mn(\frac{\partial \mathbf{u}}{\partial t} + \mathbf{u}\cdot\nabla\mathbf{u}) = -\nabla P + \nabla\cdot\sigma^{visc} + m_q n_q \nu^{coll}(\mathbf{v}-\mathbf{u}) \tag{2.2}$$

The main difference with the Navier-Stokes equations is highlighted be the presence of the Coulomb force $qn_q\mathbf{E}$ and the collision term $m_q n_q \nu^{coll}(\mathbf{v}-\mathbf{u})$. The first indicates that the electric field is responsible for the acceleration of the charged ions while the second one accounts for the momentum transfer during collisions, occurring with frequency ν, between the two species. In order to solve equation 2.1, the following assumptions are made

- Steady state.
- The convective term $\mathbf{v}\cdot\nabla\mathbf{v}$ can be neglected
- No viscous effects
- Ions are a perfect gas with $P_q = n_q k_B T$ at constant temperature

Using these assumption on 2.1, the ion velocity can be obtained

$$\mathbf{v} = \mathbf{u} + \frac{q}{m_q\nu^{coll}}\mathbf{E} - \frac{k_B T}{m_q\nu^{coll}}\nabla n_q \tag{2.3}$$

Equation 2.3 indicates that the ion velocity has three main contributions

1. Convection, due to collisions with the neutral gas
2. Acceleration due to the electric field
3. Diffusion

The last term is usually dropped as it is negligible for EHD propulsion. The term multiplying the electric field is relevant and is often indicated as μ_q and called *ion mobility*.

The expression for the ion velocity can be substituted into equation 2.2 to get

$$mn(\frac{\partial \mathbf{u}}{\partial t} + \mathbf{u} \cdot \nabla \mathbf{u}) = -\nabla P + \nabla \cdot \sigma^{visc} + q n_q \mathbf{E} \tag{2.4}$$

This shows that the neutral gas feels a Coulomb force, more properly called EHD force, that is the result of collisions with the ions.

The complete equations for the drift region are derived precisely from these assumptions. In order to simplify the notation, it is possible to indicate

- $m_q n_q = \rho_q$, space charge density
- $mn = \rho$, neutral gas mass density

In order to write the complete equations for the drift region some additional equations are needed to close the problem. Space charges will influence the electric field distribution following Maxwell's law of electromagnetism

$$\nabla \cdot \mathbf{E} = \frac{\rho_q}{\epsilon_0} \tag{2.5}$$

The ions obey the conservation of electric charge equation that, in steady state conditions, reads

$$\nabla \cdot \rho_q \mathbf{v} = 0 \tag{2.6}$$

Substituting equation 2.3 into 2.6 it is possible to obtain the complete model for the drift region

$$\begin{cases} \nabla \cdot \mathbf{E} = \rho_q/\epsilon_0 \\ \nabla \cdot \rho_q(\mu_q \mathbf{E} + \mathbf{u}) = 0 \\ \rho \mathbf{u} \cdot \nabla \mathbf{u} = -\nabla P + \mu \nabla^2 \mathbf{u} + \rho_q \mathbf{E} \end{cases} \tag{2.7}$$

2.2. Dimensional Analysis for a thruster in still air

The main physical parameters chosen to start building dimensionless quantities are

1. Applied voltage, V_a.
2. Gap, d.

The nondimensionalization of the equations is carried out starting with the following relations:

1. $\mathbf{x} = d\ \hat{\mathbf{x}}$, the reference system is made dimensionless by the gap d.
2. $\mathbf{E} = (V_a/d)\ \hat{\mathbf{E}}$, The electric field is scaled by the ratio of the applied voltage and the gap.
3. $\rho_q = \rho_0\ \hat{\rho_q}$, the space charge density is scaled by a reference value.
4. $\mathbf{u} = u_0\ \hat{\mathbf{u}}$, the hydrodynamic velocity is scaled by a reference value.
5. $P = P_0\ \hat{P}$, the pressure is scaled by a reference value.

The reference values ρ_0, u_0, P_0 are progressively exposed in what follows. The introduction of the aforementioned scaling in Eqs. 2.7 yields

$$\begin{cases} \hat{\nabla} \cdot \hat{\mathbf{E}} = \dfrac{\rho_0}{\epsilon_0 \dfrac{V_a}{d^2}} \hat{\rho_q} \\ \hat{\nabla} \cdot \hat{\rho_q} \left(\hat{\mathbf{E}} + \dfrac{u_0}{\mu_q \dfrac{V_a}{d}} \hat{\mathbf{u}} \right) = 0 \\ \hat{\mathbf{u}} \cdot \hat{\nabla} \hat{\mathbf{u}} = -\dfrac{P_0}{\rho u_0^2} \hat{\nabla} \hat{P} + \dfrac{\rho_0 V_a}{\rho u_0^2} \hat{\rho_q} \hat{\mathbf{E}} + \dfrac{\nu}{u_0 d} \hat{\nabla}^2 \hat{\mathbf{u}} \end{cases} \tag{2.8}$$

Eqs. 2.5 represent the dimensionless version of the drift region equations, provided that ρ_0, u_0, P_0 are properly defined. As for the charge density, a reference value can be defined

in such a way that the multiplicative term in the first equation has order 1:

$$\rho_0 = \epsilon_0 \frac{V_a}{d^2} \ . \tag{2.9}$$

As it will be shown later, this assumption leads to retrieve the Mott-Gurney law for the current density [26], which is a proper model for the current density in a 1D geometry.

Under the hypothesis of no external convection, only collisions between ions and neutral gas molecules are responsible for the creation of a mean flow. This suggests that the order of magnitude of the kinetic energy of the flow ρu_0^2 is comparable to the ion potential energy $\rho_0 V_a$, and leads to set

$$u_0 = \sqrt{\frac{\rho_0}{\rho} V_a} = \frac{V_a}{d} \sqrt{\frac{\epsilon_0}{\rho}} \ , \tag{2.10}$$

where Eq. 2.9 was used. The pressure reference term is similarly defined using the kinetic energy term because ionic thrusters in still air create a suction force that results in a negative pressure gradient at the inlet section, thus it is convenient to set

$$P_0 = \rho u_0^2 = \epsilon_0 \frac{V_a^2}{d^2} \ . \tag{2.11}$$

Using the aforementioned assumptions the dimensionless equations become

$$\begin{cases} \hat{\nabla} \cdot \hat{\mathbf{E}} = \hat{\rho_q} \\ \hat{\nabla} \cdot \hat{\rho_q} \left(\hat{\mathbf{E}} + R_v \hat{\mathbf{u}} \right) = 0 \\ \hat{\mathbf{u}} \cdot \hat{\nabla} \hat{\mathbf{u}} = -\hat{\nabla} \hat{P} + \hat{\rho_q} \hat{\mathbf{E}} + \dfrac{1}{Re_d} \hat{\nabla}^2 \hat{\mathbf{u}} \ , \end{cases} \tag{2.12}$$

where two new dimensionless numbers appear:

$$Re_d = \frac{u_0 d}{\nu} = \frac{V_a}{\nu} \sqrt{\frac{\epsilon_0}{\rho}} \ , \tag{2.13}$$

$$R_v = \frac{u_0}{u_i} = \frac{1}{\mu_q} \sqrt{\frac{\epsilon_0}{\rho}} \ . \tag{2.14}$$

Re_d is a Reynolds number based on the gap, appearing in the momentum equation. It is generally related to the size of the thruster through the gap, and in the present experiment ranges from 1000 to 4000 depending on the applied voltage value.

R_v, appearing in the ion transport equation, is the ratio between the reference convective velocity u_0 and the reference ion drift velocity $u_i = \mu_q V_a/d$. For a thruster in still air, $R_v \sim 10^{-2}$ and is typically negligible.

According to the previously defined reference values, the current density can be made dimensionless in the following form:

$$\mathbf{j} = \rho_q \left(\mu_q \mathbf{E} + \mathbf{u}\right) = \epsilon_0 \mu_q \frac{V_a^2}{d^3} \hat{\mathbf{j}} \,, \tag{2.15}$$

where the dimensionless quantity is

$$\hat{\mathbf{j}} = \hat{\rho_q} \left(\hat{\mathbf{E}} + \frac{1}{\mu_q} \sqrt{\frac{\epsilon_0}{\rho}} \hat{\mathbf{u}} \right) \,. \tag{2.16}$$

In 2.3 it will be shown that in 1D, under suitable assumptions, the dimensionless current density becomes $\hat{j} = 9/8$, which in Eq. (2.15) yields the dimensional functional form of the current density predicted by the Mott-Gurney law [26].

Using the reference values defined above for the local quantities, it is possible to compute reference values for the integral quantities.

2.2.1. Thrust

The thrust force generated is defined as the integral of the EHD force density. In a 2D framework as in Fig. 1.1, the derived value is a thrust per unit span, where the span b extends along the z direction, normal to the xy plane defined in figure:

$$\frac{T}{b} = \int_\Omega \rho_q E_x \, \mathrm{d}\Omega \tag{2.17}$$

where E_x is the x component of $\mathbf{E}$ and Ω is the 2D section in the xy plane of a volume extending along the z direction with constant cross section. Using the chosen reference values, the thrust integral becomes

$$\frac{T}{b} = \epsilon_0 \frac{V_a^2}{d} \int_{\hat{\Omega}} \hat{\rho}_q \hat{E}_x \, \mathrm{d}\hat{\Omega} = \epsilon_0 \frac{V_a^2}{d} C_T \tag{2.18}$$

and the thrust coefficient C_T turns out as a dimensionless thrust integral. Besides thrust, another force must be considered: the aerodynamic drag D on the electrodes (negligible for the emitters in the present study). The difference between thrust and drag may be

called *effective thrust*:

$$T_e = T - D \ . \tag{2.19}$$

Using the aerodynamic scaling laws, it is possible to express this quantity through a dimensionless coefficient:

$$\frac{T_e}{b} = \epsilon_0 \frac{V_a^2}{d} C_T - \frac{1}{2}\rho u_0^2 \ c \ C_D = \epsilon_0 \frac{V_a^2}{d} \left(C_T - \frac{1}{2}\frac{c}{d} C_D \right) = \epsilon_0 \frac{V_a^2}{d} \ C_{Te} \ . \tag{2.20}$$

The *effective thrust coefficient* $C_{Te} = C_T - \frac{1}{2}(c/d)C_D$ inherently accounts also for the aerodynamic drag. It is interesting to observe that the efficiency, defined as the ratio between the electrical thrust and the drag [29], increases as the ratio c/d decreases, i.e. it increases by shortening the airfoil chord with a given gap:

$$\theta = \frac{T}{D} = 2 \ \frac{d}{c} \ \frac{C_T}{C_D} \ . \tag{2.21}$$

2.2.2. Electrical power

The power consumption per unit span can be computed using the integral

$$\frac{P}{b} = \int_\Omega \mathbf{j} \cdot \mathbf{E} \ \mathrm{d}\Omega \ . \tag{2.22}$$

The application of the presented scaling yields

$$\frac{P}{b} = \mu_q \epsilon_0 \frac{V_a^3}{d^2} \int_{\hat{\Omega}} \hat{\mathbf{j}} \cdot \hat{\mathbf{E}} \ \mathrm{d}\hat{\Omega} \ = \ \mu_q \epsilon_0 \frac{V_a^3}{d^2} \ C_P \tag{2.23}$$

where C_P is the power coefficient.

2.2.3. Mechanical power

The mechanical power transferred to the gas is the volume integral of the mechanical power of the EHD force

$$\frac{P_u}{b} = \int_\Omega \mathbf{u} \cdot \rho_q \mathbf{E} \ \mathrm{d}\Omega \ . \tag{2.24}$$

The latter is scaled as

$$\frac{P_u}{b} = \epsilon_0 \frac{V_a^3}{d^2} \sqrt{\frac{\epsilon_0}{\rho}} \int_{\hat{\Omega}} \hat{\rho}_q \hat{\mathbf{u}} \cdot \hat{\mathbf{E}} \, \mathrm{d}\hat{\Omega} = \epsilon_0 \frac{V_a^3}{d^2} \sqrt{\frac{\epsilon_0}{\rho}} \, C_{Pu} \tag{2.25}$$

where C_{Pu} is the mechanical power coefficient.

2.2.4. Performance parameters

Several performance parameters can be put in dimensionless form according to the previous scaling, always accounting for the drag effects.

The effective thrust to power ratio can be expressed as

$$\frac{T_e}{P} = \frac{\mu_q d}{V_a} \frac{C_{Te}}{C_P} = \frac{\mu_q d}{V_a} \, C_{TPe} \, . \tag{2.26}$$

A meaningful frontal area $A = S \; b$ can be defined, with reference to Fig. 1.1, as (frontal size $\times$ span) or (spacing $\times$ span) on the yz plane. In this way, an effective surface thrust density can be defined as

$$\frac{T_e}{A} = \epsilon_0 \frac{V_a^2}{Sd} C_{Te} = \epsilon_0 \frac{V_a^2}{d^2} \frac{d}{S} \, C_{Te} = \epsilon_0 \frac{V_a^2}{d^2} \, C_{TAe} \, , \tag{2.27}$$

having introduced the effective surface thrust density coefficient

$$C_{TAe} = \frac{d}{S} C_{Te} \, . \tag{2.28}$$

Once a suitable reference area has been defined, the extension to an effective volumetric thrust density is straightforward by considering a volume $A \; l$, where l is the thruster size (or a meaningful length) along the x direction:

$$\frac{T_e}{Al} = \epsilon_0 \frac{V_a^2}{Sld} C_{Te} = \epsilon_0 \frac{V_a^2}{d^3} \frac{d^2}{Sl} C_{Te} = \epsilon_0 \frac{V_a^2}{d^3} C_{TVe} \, , \tag{2.29}$$

having introduced the effective volumetric thrust density coefficient

$$C_{TVe} = \frac{d^2}{Sl} C_{Te} \tag{2.30}$$

Finally, the mechanical-to-electrical power ratio can be introduced as electro-mechanical efficiency, describing the fraction of electrical energy that is converted into mechanical

energy:

$$\eta = \frac{P_u}{P} = \frac{1}{\mu_q}\sqrt{\frac{\epsilon_0}{\rho}}\frac{C_{Pu}}{C_P} \,, \tag{2.31}$$

and in dimensionless form becomes C_{Pu}/C_P.

All the scaled quantities are presented in the summary tables 2.1 and 2.2.

Table 2.1: Integral quantities

Name	Symbol	Reference Value	Dimensionless Coefficient
Effective Thrust	$\frac{T_e}{b}$	$\epsilon_0\frac{V_a^2}{d}$	C_{Te}
Electrical Power	$\frac{P}{b}$	$\mu_q\epsilon_0\frac{V_a^3}{d^2}$	C_P
Mechanical Power	$\frac{P_u}{b}$	$\epsilon_0\frac{V_a^3}{d^2}\sqrt{\frac{\epsilon_0}{\rho}}$	C_{Pu}

Table 2.2: Performance parameters

Name	Symbol	Reference Value	Dimensionless Coefficient
Thrust to Power Ratio	$\frac{T_e}{P}$	$\frac{\mu_q d}{V_a}$	C_{TPe}
Surface Thrust Density	$\frac{T_e}{A}$	$\epsilon_0\frac{V_a^2}{d^2}$	C_{TAe}
Volumetric Thrust Density	$\frac{T_e}{Al}$	$\epsilon_0\frac{V_a^2}{d^3}$	C_{TVe}
Electro-mechanical Efficiency	$\frac{P_u}{P}$	$\frac{1}{\mu_q}\sqrt{\frac{\epsilon_0}{\rho}}$	$\frac{C_{Pu}}{C_P}$

2.3. 1D Theory for a thruster in still air

The scaling model of §2 is applied here to a simple 1D geometry, with the aim of solving the scaled equations in this framework and obtain relevant scaling laws for the performance parameters.

The 1D geometry can be imagined as an emitter plane facing a parallel collector plane, separated by a gap d. The x axis spans from the emitters $x = 0$ to the collectors $x = d$, or $0 \leq \hat{x} \leq 1$ in the scaled domain. To model such a system, Kapztov's hypothesis [15]

is used to describe the ionization region using Peek's boundary condition [27] and setting the dimensionless electric field at the emitter as

$$\hat{E}(0) = \frac{E_i d}{V_a} = \frac{V_i}{V_a} = \hat{V}^{-1} \,, \tag{2.32}$$

where the inception voltage and field are related by $V_i = E_i d$ and $\hat{V}$ is the scaled voltage defined in Eq. (**??**).

2.3.1. Solution of the 1D equations

Eqs. (2.5) for electric field and current are reduced here to the case of the 1D geometry:

$$\begin{cases} \dfrac{\partial \hat{E}}{\partial \hat{x}} = \hat{\rho}_q \\ \dfrac{\partial}{\partial \hat{x}}\ \hat{\rho}_q \hat{E} = 0 \,. \end{cases} \tag{2.33}$$

The second equation can be integrated to yield an integration constant which is the dimensionless current density

$$\hat{\rho}_q \hat{E} = \hat{\jmath} \,, \tag{2.34}$$

and substituting this expression in the first Eq. (2.33) it is obtained

$$\hat{E}\ \frac{\partial \hat{E}}{\partial \hat{x}} = \hat{\jmath} \,. \tag{2.35}$$

Using the condition $\hat{E}(0) = V_i/V_a = \hat{V}^{-1}$ this equation can be solved leading to

$$\hat{E}(\hat{x}) = \sqrt{2\ \hat{\jmath}\ \hat{x} + \hat{V}^{-2}} \,. \tag{2.36}$$

This expression for the electric field can be integrated on the scaled domain [0,1]: the left hand term becomes the potential difference across the gap, which in dimensionless form is $V_a/V_a = 1$, and the result is the equation

$$1 = \frac{-\hat{V}^{-3} + (2\hat{\jmath} + \hat{V}^{-2})^{3/2}}{3\hat{\jmath}} \,, \tag{2.37}$$

which admits the following closed form solution for $\hat{\jmath} \geq 0$:

$$\hat{\jmath} = \frac{9 - 12\hat{V}^{-2} + \sqrt{(3 - 2\hat{V}^{-1})^3\ (3 + 6\hat{V}^{-1})}}{16} \,. \tag{2.38}$$

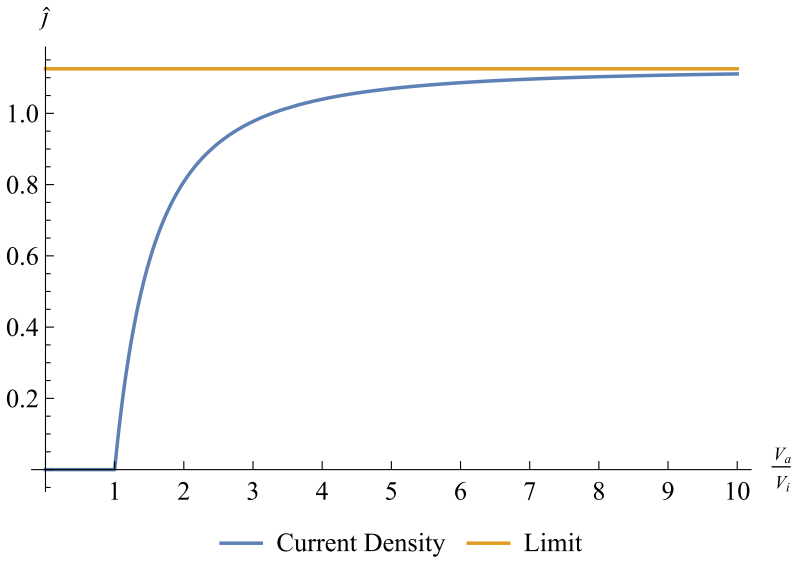

Figure 2.1: Current density curve

This function, plotted in Fig. 2.1, has distinct asymptotic behaviours in the low and high voltage limits. When the voltage starts rising from the inception voltage, $(\hat{V}-1)$ is small and the current density trend is nearly linear,

$$\hat{\jmath} = 2\ (\hat{V}-1) + O[\ (\hat{V}-1)^2]\ . \tag{2.39}$$

When the voltage is high, the function has the asymptotic behaviour

$$\hat{\jmath} = \frac{9}{8} - \frac{3}{2}\hat{V}^{-2} + O(\hat{V}^{-3})\ , \tag{2.40}$$

so that when $\hat{V} \to \infty$, i.e. under the choked condition $E(0) \to 0$, the Mott-Gurney law $\hat{\jmath} = 9/8$ is correctly recovered [22, 26].

2.3.2. Thrust and electrical power coefficients

In 1D, the integral for the thrust reads

$$C_T = \int_0^1 \hat{\rho}_q \hat{E}\ \mathrm{d}\hat{x} = \hat{\jmath}\ . \tag{2.41}$$

The ideal thrust coefficient without drag is therefore equal to the dimensionless current density, constant on the domain. The electrical power coefficient integral is

$$C_P = \int_0^1 \hat{\jmath}\ \hat{E}\ \mathrm{d}\hat{x} = \hat{\jmath} \int_0^1 \hat{E}\ \mathrm{d}\hat{x} = \hat{\jmath} = C_T\ . \tag{2.42}$$

Hence, for a 1D configuration

$$C_{TP} = \frac{C_T}{C_P} = 1. \tag{2.43}$$

2.4. Dimensional Analysis with the addition of a Mean Flow

The issue of the addition of the mean flow is a crucial aspect to consider when examining the motion of a thruster in relation to a still air volume. It is essential to understand the impact that this addition has on the generated thrust force and the power consumption of the thruster.

The velocity, denoted as U, of the moving thruster is determined by the equilibrium condition $T(U) - D(U) = 0$, where $T(U)$ is the thrust force generated by the thruster and $D(U)$ is the drag force experienced by the vehicle.

It is important to note that analyzing the functional form of $T(U)$ requires expensive wind tunnel testing. Hence, it is imperative to study what the dimensionless model can tell us about this dependence.

To construct suitable reference values for the dimensionless model, the gap is chosen as the main geometric scaling length, and the applied voltage is chosen as the main electrical quantity. The mean flow velocity can be scaled with a u_∞ term that represents the order of magnitude of such velocity.

$$\begin{cases} \hat{\nabla} \cdot \hat{\mathbf{E}} = \dfrac{\rho_0}{\epsilon_0 \dfrac{V_a}{d^2}} \hat{\rho}_q \\ \hat{\nabla} \cdot \hat{\rho}_q \left(\hat{\mathbf{E}} + \dfrac{u_\infty}{\mu_q \dfrac{V_a}{d}} \hat{\mathbf{u}} \right) = 0 \\ \hat{\mathbf{u}} \cdot \hat{\nabla} \hat{\mathbf{u}} = -\dfrac{P_0}{\rho u_\infty^2} \hat{\nabla} \hat{P} + \dfrac{\rho_0 V_a}{\rho u_\infty^2} \hat{\rho}_q \hat{\mathbf{E}} + \dfrac{\nu}{u_\infty d} \hat{\nabla}^2 \hat{\mathbf{u}} \end{cases} \tag{2.44}$$

The first dimensionless number, R_v, represents the ratio between the neutral gas and ion velocity and indicates the weight of the convective term in the equations. This number is significant because it helps us understand the importance of the convective term in relation to the other terms in the equations and its effect will be thoroughly explored. The second dimensionless number, Re_d, represents the Reynolds number based on the

convective velocity and the gap.

$$\begin{cases} \hat{\nabla}\cdot\hat{\mathbf{E}} = \hat{\rho}_q \\ \hat{\nabla}\cdot\hat{\rho}_q\left(\hat{\mathbf{E}} + R_v\hat{\mathbf{u}}\right) = 0 \\ \hat{\mathbf{u}}\cdot\hat{\nabla}\hat{\mathbf{u}} = -\hat{\nabla}\hat{P} + \left(\dfrac{1}{R_v}\dfrac{1}{\mu_q}\sqrt{\dfrac{\epsilon_0}{\rho}}\right)^2\hat{\rho}_q\hat{\mathbf{E}} + \dfrac{1}{Re_\infty}\hat{\nabla}^2\hat{\mathbf{u}} \end{cases} \tag{2.45}$$

Upon examining the velocity ratio dimensionless number, R_v, we can see that it acts as a denominator in the volumetric EHD force. This implies that the addition of a mean flow results in a reduction of the significance of this term.

This observation is intuitive since in the still case, it was the collisions between ions and neutral gas that generated the air flow. However, in the presence of a mean flow, the airflow is already present, and the effect of collisions becomes less evident in the equations as the velocity is increased.

Therefore, the addition of a mean flow has a damping effect on the volumetric EHD force, making it less significant.

2.5. 1D Theory with a mean flow

Equations are now simplified in the case of a 1D motion. The conservation of mass in the case of a 1D flow show that this velocity is equal everywhere in the domain and it is assumed to be equal to its reference value, u_∞. The addition to this hypothesis yields the following drift region equations

$$\begin{cases} \dfrac{\partial}{\partial\hat{x}}\hat{E} = \hat{\rho}_q \\ \dfrac{\partial}{\partial\hat{x}}\hat{\rho}_q\left(\hat{E} + R_v\right) = 0 \end{cases} \tag{2.46}$$

After integrating the two differential equations over the interval [0,1] and applying Peek's boundary condition, we obtain an algebraic equation that describes the current density as a function of the dimensionless voltage and the dimensionless velocity ratio.

$$1 = \frac{-\left(\hat{V}^{-1} + R_v\right)^3 + \sqrt{\left(\left(\hat{V}^{-1} + R_v\right)^2 + 2\hat{\jmath}\right)^3}}{3\hat{\jmath}} - R_v \tag{2.47}$$

The algebraic equation that describes the current density as a function of the dimensionless voltage and the dimensionless velocity ratio has a rather complex closed-form solution, which is crucial for understanding the behavior of the system since the dimensionless current is equal to the power coefficient. This solution is conveniently presented in Figure 2.2.

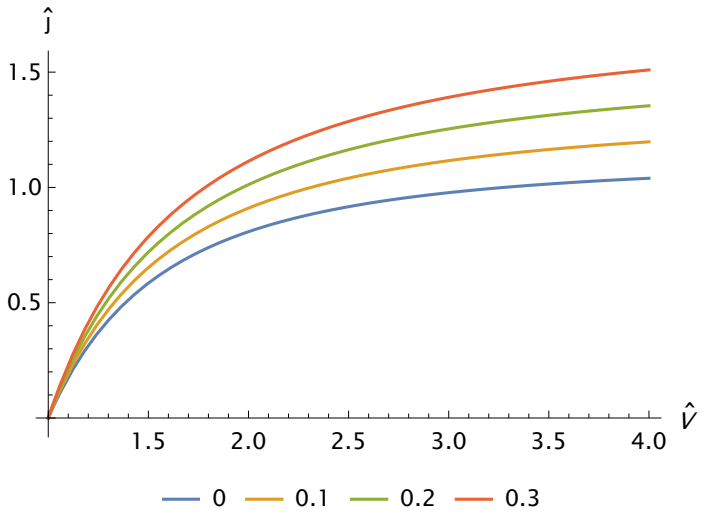

Figure 2.2: Current density dependence on the scaled voltage for different values of the convective term.

Upon examining Figure 2.2, it becomes apparent that the dimensionless current increases significantly as the effect of the convective term is amplified. This increase can be attributed to the fact that the presence of a mean flow will extract more ions from the ionization region, leading to a higher current consumption.

The addition of a mean flow alters the ion flow behavior, resulting in more ions being expelled from the thruster's ionization region. As a result, a higher current is required to maintain the desired thrust force. This effect is more pronounced at higher values of the dimensionless velocity ratio, indicating that the velocity of the thruster relative to the still air volume has a significant impact on its power consumption.

2.5.1. Thrust coefficient

The thrust coefficient was defined as the volumetric integral of the thrust density term. In a 1D formulation, this coefficient is equivalent to a surface thrust density and the volumetric integral reduces to a line integral.

$$C_T = \int_0^1 \hat{\rho}_q \hat{E} \, \mathrm{d}\hat{\mathrm{x}} = \hat{\jmath} \int_0^1 \frac{\hat{\mathrm{E}}}{\hat{\mathrm{E}} + \mathrm{R_v}} \, \mathrm{d}\hat{\mathrm{x}} \tag{2.48}$$

This integral admits a, rather complex, closed form solution, which is not reported for brevity.

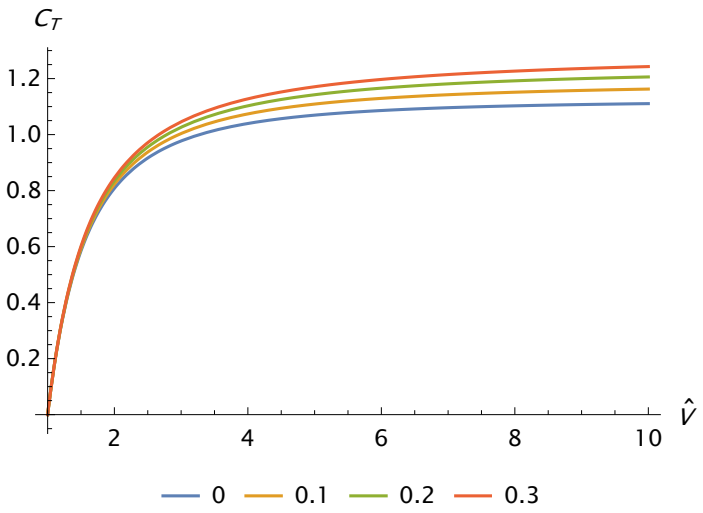

Figure 2.3: Thrust coefficient dependence on the scaled voltage for different values of the convective term, R_v.

Figure 2.3 reports the thrust coefficient functional dependence on the dimensionless voltage for different values of the convective term, R_v. It is possible that the behaviour of this value is similar to the case of the thruster in still air as it exhibits similar low and high voltage limits. Increasing the convective term increases the thrust coefficient but this increase is smaller if compared to the power coefficient; moreover, the actual thruster suffers from the addition of aerodynamic drag which increases as the mean flow velocity is increased.

2.5.2. Thrust to Power coefficient

The thrust to power coefficient is defined as the ration of the thrust coefficient and the power coefficient. The power coefficient asymptotic values increases significantly, being equal to the current density coefficient, as the mean flow value increases whereas the thrust coefficient undergoes a less significant increase.

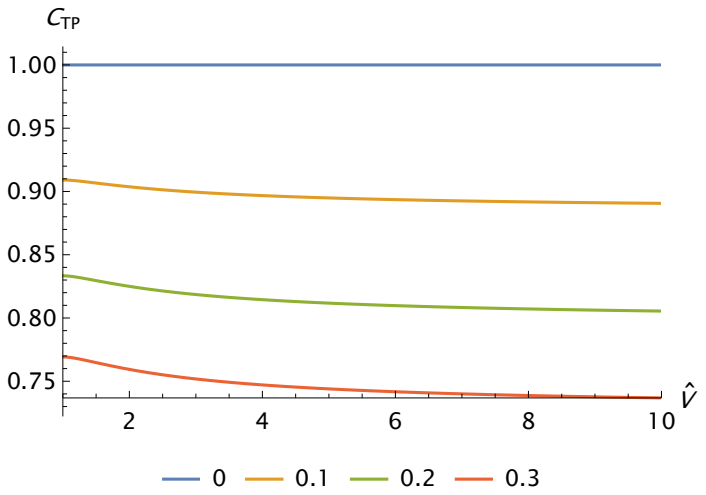

Figure 2.4: Thrust to Power coefficient dependence on the scaled voltage for different values of the convective term, R_v.

Figure 2.4 shows the behaviour of the thrust to power coefficient as a function of the dimensionless voltage and for different convective term values. It is possible to conclude that the 1D model predicts a substantial loss in the thrust to power. This is also worsened by the presence of aerodynamic drag which reduces the generated thrust.

These results are of critical importance for any future application of this technology. A reduction of the total thrust to power means that, for a given power requirement, the thruster will be able to generate less thrust as the velocity increases greatly limiting the speed of ionic thrusters.

2.6. 2D Theory

The dimensionless model can be applied to a study case in which the geometry is two dimensional. It should be remarked that only a few closed form solution exist and that a general solution for the wire-airfoil case is not possible. The goal of this section is not to solve the 2D drift region equations but to express the performance parameters as integrals on the cathode shape. The thrust and power coefficients are defined as integrals on the entire volume of the thruster, and this expression is not useful. Expressing these volumetric integrals as surface integrals, on the cathode shape, would be more useful since it would create a link between these indicators and the cathode shape, which is required for this thesis. The geometry that will be studied is depicted in Figure 2.5.

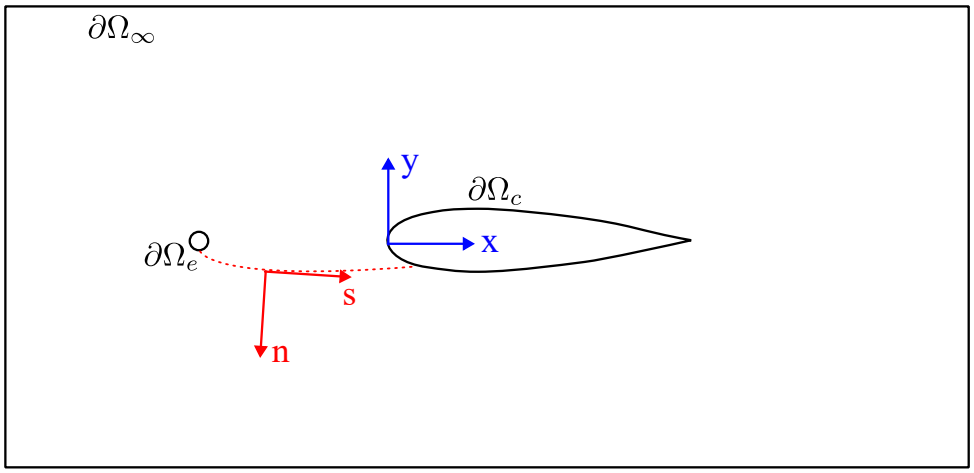

Figure 2.5: 2D geometry framework. The cartesian reference system is shown in blue and the intrinsic reference system is shown in red.

A single emitter-collector configuration, immersed in an infinitely large domain, will be studied. The emitter boundary is called, $\partial\Omega_e$ and the cathode boundary will be called $\partial\Omega_c$. To solve the integrals, we will assume that the cathode shape, in 2D it is a curve, can be parameterized using a free coordinate, u, and the curve $(x_c(u), y_c(u))$. It is also necessary to introduce the *intrinsic reference system* which is the reference system aligned with a current filament. The 2D equations read

$$\begin{cases} \hat{\nabla} \cdot \hat{\mathbf{E}} = \hat{\rho_q} \\ \hat{\nabla} \cdot \hat{\mathbf{j}} = 0 \, . \end{cases} \tag{2.49}$$

2.6.1. Power Coefficient

The power coefficient is defined as the integral of the dot product between the current density and the electric field. Using the properties of the divergence we can write

$$\hat{\nabla} \cdot \hat{\mathbf{j}}\hat{V} = \hat{\mathbf{j}} \cdot \hat{\nabla}\hat{V} + \hat{V}\hat{\nabla} \cdot \hat{\mathbf{j}} = \hat{\mathbf{j}} \cdot \hat{\mathbf{E}} \tag{2.50}$$

In this equation, the definition of the electric field and the zero divergence of the current density have been used. It is therefore possible to compute the power coefficient using

$$C_P = \int_{\hat{\Omega}} \hat{\mathbf{j}} \cdot \hat{\mathbf{E}} \, \mathrm{d}\hat{\Omega} = \int_{\hat{\Omega}} \hat{\nabla} \cdot \hat{\mathbf{j}}\hat{V} \, \mathrm{d}\hat{\Omega} = \oint_{\partial\hat{\Omega}} \hat{V}\hat{\mathbf{j}} \cdot \hat{\mathbf{n}} \, \mathrm{d}\partial\hat{\Omega} \, . \tag{2.51}$$

The surface integral can be decomposed into the integral on the emitter surface, the

cathode surface and the boundary at infinity. The latter vanishes because at infinity the current density is zero.

$$C_P = \int_{\partial\hat{\Omega}_e} \hat{V}\hat{\mathbf{j}} \cdot \hat{\mathbf{n}} \, \mathrm{d}\partial\hat{\Omega} + \int_{\partial\hat{\Omega}_c} \hat{V}\hat{\mathbf{j}} \cdot \hat{\mathbf{n}} \, \mathrm{d}\partial\hat{\Omega} \, . \tag{2.52}$$

To further simplify the integral we can use the fact that the potential at the collector surface is zero therefore the integral vanishes and is one at the emitter. Actually, it is also possible to add an arbitrary constant to such field without changing the solution. We could also assume that the potential is zero at the emitter and -1 at the collector. It is therefore possible to express this integral both at the emitter and at the cathode surface.

$$C_P = \int_{\partial\hat{\Omega}_e} \hat{\mathbf{j}} \cdot \hat{\mathbf{n}} \, \mathrm{d}\partial\hat{\Omega} = -\int_{\partial\hat{\Omega}_c} \hat{\mathbf{j}} \cdot \hat{\mathbf{n}} \, \mathrm{d}\partial\hat{\Omega} \, . \tag{2.53}$$

The latter is the most useful definition since it connects the current density distribution at the cathode surface with the shape of the cathode. The minus sign is due to the fact that the current is directly towards the collector and can be rewritte using the following

$$C_P = \int_{\partial\hat{\Omega}_c} \hat{j} \, \mathrm{d}\partial\hat{\Omega} \, . \tag{2.54}$$

2.6.2. Thrust Coefficient

The computation of the thrust coefficient integral is more involved than the one concerning the power coefficient. It is possible to use the electromagnetic stress tensor to use the divergence theorem as done previously but it is not possible to make the integral at the emitter surface vanish hence it is not useful for our purposes. It is, however, more convenient to use the fact that the current filaments start at the emitter surface and end at the cathode surface. The volumetric integral can therefore be performed integrating the quantities along a current filament, first, and then at the cathode surface.

$$C_T = \int_{\hat{\Omega}} \hat{\rho}_q \hat{E}_x \, \mathrm{d}\hat{\Omega} = \int_{\partial\hat{\Omega}_c} \int_s \hat{\rho}_q \hat{E}_x \, \mathrm{d}s \, \mathrm{d}\partial\hat{\Omega} \, . \tag{2.55}$$

Lets focus on the current filament integral. It is possible to express this integral as

$$\int_s \hat{\rho}_q \hat{E}_x \, \mathrm{d}s = \int_s \hat{\rho}_q \hat{E}_s \cos(\theta_\mathrm{s}) \, \mathrm{ds} = \int_\mathrm{s} \hat{j} \cos(\theta_\mathrm{s}) \, \mathrm{ds} \tag{2.56}$$

In this case we have separated the intrinsic component of the electric field and the projection on the x-axis. The integral of the cosine angle would yield the x-axis length of the current filament.

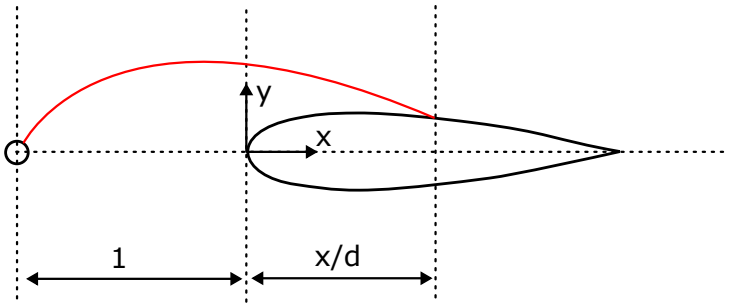

Figure 2.6: Lengths and dimensions of the 2D geometry

Using the reference frames introduced in Figure 2.6 we can say that

$$\int_s \cos(\theta_s)\ \mathrm{ds} = \Delta \mathrm{L_x} = 1 + \mathrm{x(u)/d}\ , \tag{2.57}$$

We can use this fact to integrate the current filament integral by parts

$$\int_s \hat{\jmath}\ \cos(\theta_s)\ \mathrm{ds} = \hat{\jmath}\left(1 + \frac{\mathrm{x(u)}}{\mathrm{d}}\right) - \int_s \frac{\partial \hat{\jmath}}{\partial \mathrm{s}}\ \cos(\theta_s)\ \mathrm{ds}\ . \tag{2.58}$$

The last integral vanishes because the derivative of the current density in the intrinsic frame corresponds to the divergence of the current density field expressed in the intrinsic frame which is zero. Hence we get the expression of the thrust coefficient integral

$$C_T = \int_{\partial \hat{\Omega}_c} \hat{\jmath}\left(1 + \frac{x(u)}{d}\right)\ \mathrm{d}\partial\hat{\Omega}\ . \tag{2.59}$$

This equation is similar to the one of the power coefficient but weighs the current density by a factor which increases as the distance from the emitter is increased. This is natural since, the more an ion travels, the more collisions it makes with neutral gas molecules.

2.7. Simple Analytical solutions

This section is devoted to the investigation of simple closed form 2D solutions which assume a particular distribution of the current density at the cathode surface and compute the power and thrust coefficient.

2.7.1. Wire to Infinite Plate

The case of a pin-plate configuration was extensively studied by Warburg and Sigmond [14]. The functional dependence provided is

$$\hat{\jmath} = \frac{\cos^4(\theta)}{1 + \frac{1}{2}\sin^2(\theta)} \tag{2.60}$$

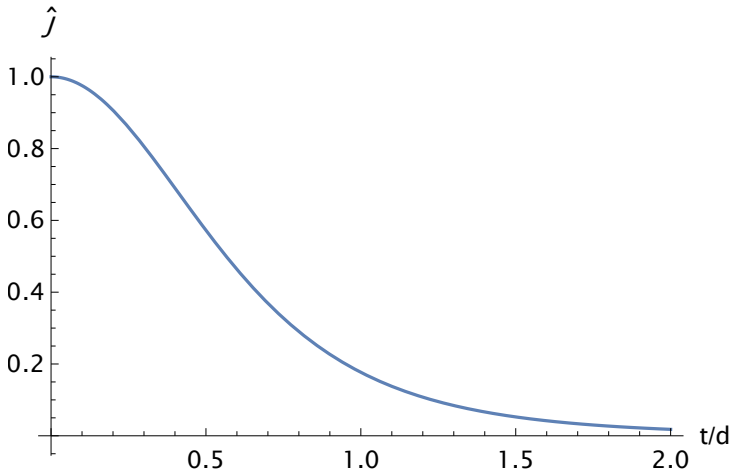

Figure 2.7: Warburg's 2D current distribution.

Where θ is the angle between the centerline and the line connecting the electrode to a particular plate point. In this case, the cathode surface can be easily parameterized, with a reference to the system used in Figure 2.6, using $x(u) = 0, y(u) = u$. The integrals read

$$C_P = C_T = \int_{\partial\hat{\Omega}_c} \hat{\jmath}\, \mathrm{d}\partial\hat{\Omega} = \int_{-\infty}^{\infty} \hat{\jmath}\sqrt{x'(u)^2 + y'(u)^2}\, \mathrm{d}\hat{u} = \frac{4}{3}\,. \tag{2.61}$$

This result is important because it shows that, in the case of a wire to infinite plate configuration, the power coefficient is able to reach values higher than the 1D limit (which is $9/8 = 1.2$). In this case, the limit provides a power coefficient equal to 1.33. In the case of a finite plate, if this integral is computed up to a certain point, the coefficients will be lower. In particular for a plate of whose height is half the gap, the coefficients will be 0.47.

2.7.2. Wire to Cylinder

The wire to cylinder case is an interesting 2D configuration. The cylinder is not an aerodynamic shape but it can be seen as a prototype for more sophisticated airfoil shapes. The radius of cylinder is R. Moronis et al. provide the current distribution at the cathode surface as a function of the angle, ϕ, and a dimensionless parameter called a, which, for a 30 µm emitter is

$$a = \left(\frac{r_e}{d}\right)^{0.0083} + \left(\frac{R}{d}\right)^{0.7} = 0.942 + \left(\frac{R}{d}\right)^{0.7} \tag{2.62}$$

The dimensionless current distribution is

$$\hat{\jmath} = \cosh^{-3a}(\phi) \tag{2.63}$$

Using this equation the power and thrust coefficient integrals can be computed using the proposed integrals

$$C_P = 2\frac{R}{d}\int_0^{\pi} \hat{\jmath}\, \mathrm{d}\phi \tag{2.64}$$

$$C_T = 2\frac{R}{d}\int_0^{\pi} \hat{\jmath}\left(1 + \frac{R}{d}\left(1 + \cos\left(\pi - \phi\right)\right)\right)\, \mathrm{d}\phi\ . \tag{2.65}$$

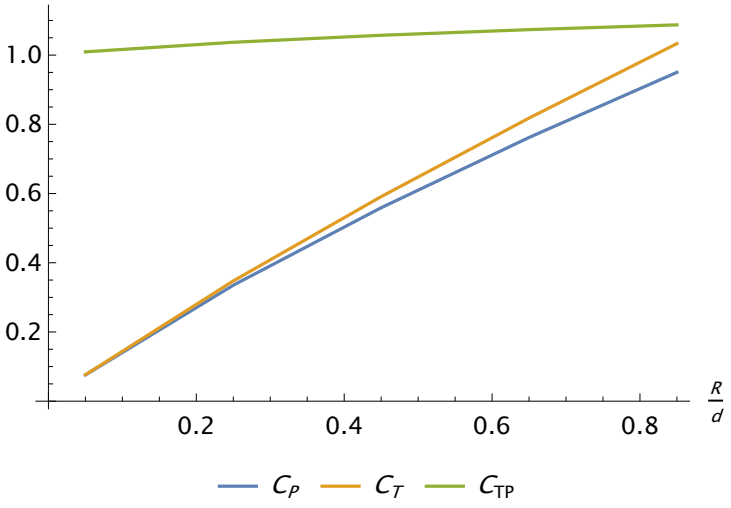

Figure 2.8: Performance indicators for the wire to cylinder case.

Figure 2.8 shows the behaviour of the main performance parameters, computed from the

surface integrals, as a function of the dimensionless cylinder radius R/d. These data, coming from numerical correlations, are not valid as the cylinder radius increases indefinitely hence, when $R/d \to \infty$, the curves do not approach the flat plate limit. It is however clear that increasing the collector radius will increase both the power and thrust coefficients. To account for aerodynamic drag we should use the cylinder Reynolds number which can be computed using the scaling model presented in previous sections.

The drag coefficient can be computed using the following formula, which is valid for the Reynolds numbers used in this work

$$C_D = \frac{24}{\mathrm{Re}} \left(1 + 0.15\ \mathrm{Re}^{0.687}\right) + 0.42 \tag{2.66}$$

The aerodynamic drag contribution can therefore be added to the thrust coefficient term using Equation 2.20.

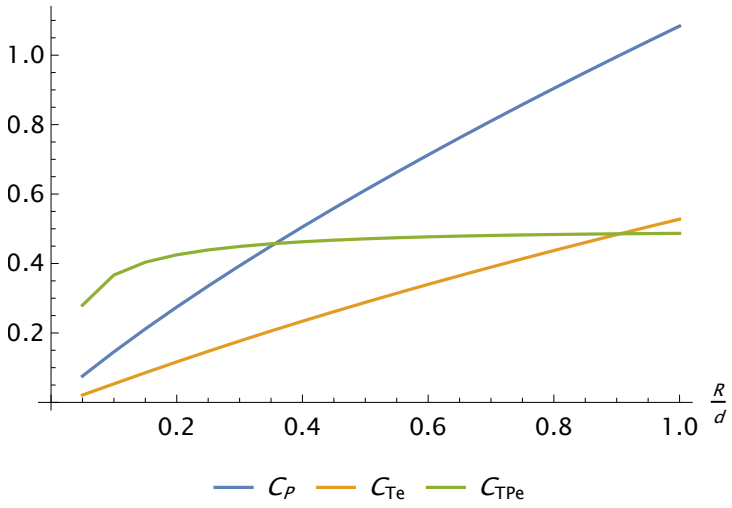

Figure 2.9: Performance indicators for the wire to cylinder case with the addition of aerodynamic drag.

With the addition of aerodynamic drag the thrust coefficient is much lower. Tho order of magnitude of the dimensionless coefficient shows both qualitative and quantitative agreement with the experimental data provided in the next sections.

This method allows for fast computations of the performance indicators for any shape, provided that a suitable definition of the functional form is provided. Numerical computations and experimental measurements can provide some empirical fitting of the current

distribution which can be used by a fast optimization routine to select the best shape given a required gap to voltage ratio.

3 | Experimental Setup

A custom made experimental setup was employed in order to perform direct thrust and electric measurements.

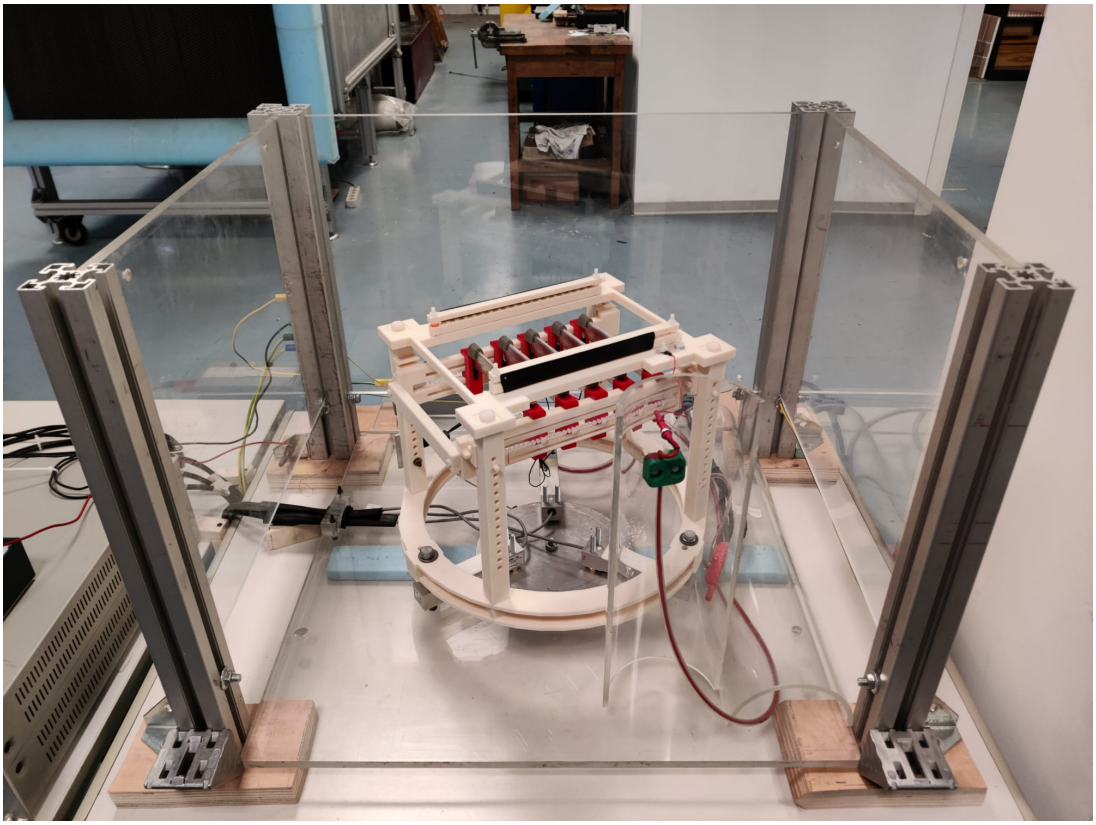

Figure 3.1: Photo of the experimental setup

The test rig, already used in a previous work [2], is depicted in Fig. 3.2 and its components present major modifications in the support structures. The results are analysed in a reference system consistent with Fig. 1.1, with axes referred to the collectors; thus the directions are x (chordwise), y (normal to the airfoils chords) and z (spanwise).

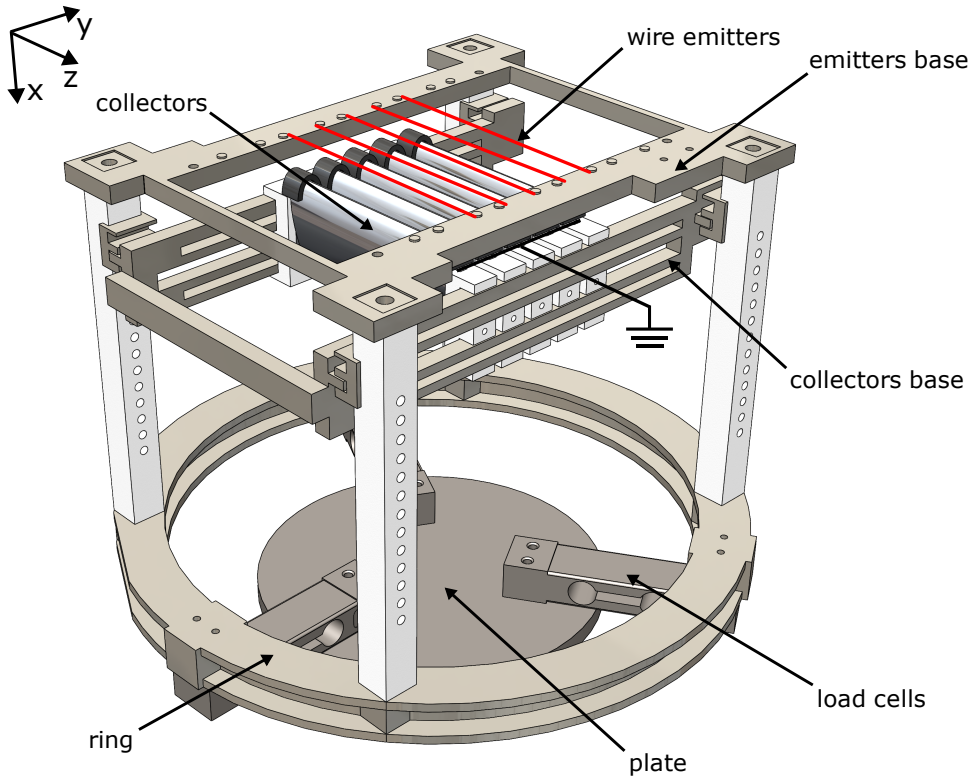

Figure 3.2: Experimental Setup

3.1. Setup Components

The test rig was constructed using 3D printing technology, specifically the Fortus 450MC and Delta Wasp 2040 printers, which utilized Acrylic Styrene Acrylonitrile (ASA) and Polylactide (PLA) as building materials. These materials were chosen for their strong mechanical properties and ease of use in the printing process.

3.1.1. Ring and Load Cells

The ring serves as a circular and rigid structural component that plays a crucial role in supporting the thruster structure and transferring loads to the load cells.

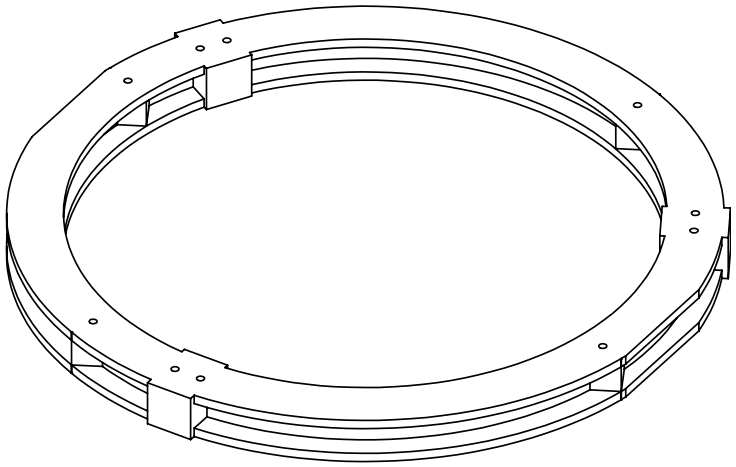

Figure 3.3: Structural Ring

PWC6 load cells by HBM were used to measure the load. These load cells guarantee a precision of 0.1 g in an absolute measurement. The full scale load is 0.75 kg. The load cells are fed with an input DC voltage of 10 V by a signal conditioner that serves also the purpose of amplifying the output voltage. This instrument is calibrated to produce a 0 V output when unloaded and a gain of 10 $\frac{\text{V}}{\text{kg}}$.

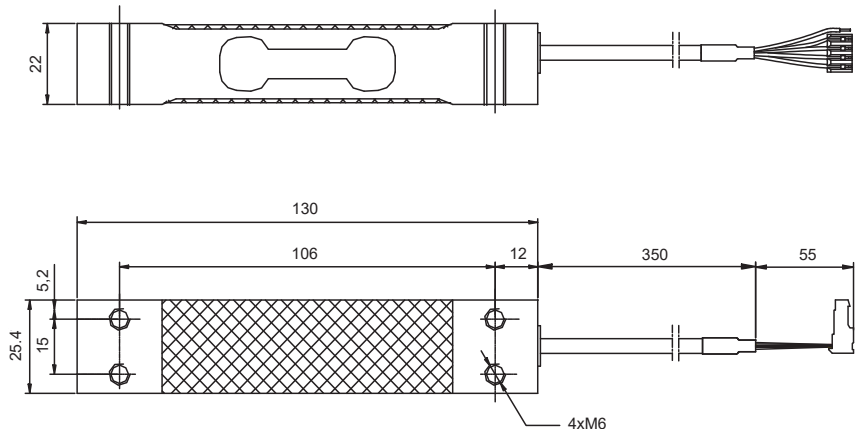

Figure 3.4: Technical drawing of the PW6C Load Cells (dimensions are given in mm)

The load cells are conveniently positioned in a radial configuration on a grounded metal plate. By distributing the loads uniformly through the ring and onto the load cells, the test rig is able to accurately measure the forces and torques generated by the thruster. This configuration also ensures that the test results are reliable and consistent, which is essential for conducting accurate experiments and obtaining meaningful data.

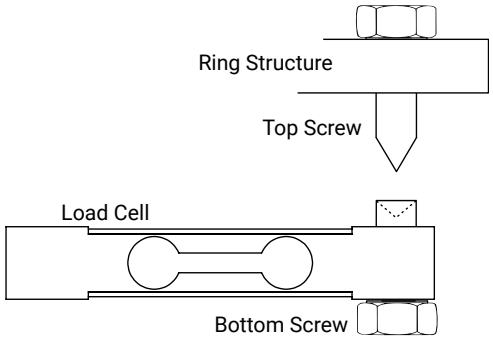

Figure 3.5: Detail of the mounting mechanism (not to scale)

To enhance the accuracy and precision of force transfer in the test rig, a new mounting system was developed and is illustrated in Figure 3.7. Each load cell is equipped with a screw featuring a 90° conical hole at the end. Three screws with cone-shaped ends that have a 60° angle are then threaded in a radial arrangement onto the ring structure. The structure is then placed on top of the load cell, so that the top and bottom screws make contact with the load cell's screw. This setup promotes repeatability in the positioning process and improves the measurement precision. By ensuring that contact and force transmission occur at a single point, which is a fixed distance from the load cell's mounting point, the lever arm is kept constant, leading to more consistent and accurate results.

3.1.2. Airfoil Collectors

The cathodes consist of 5 NACA airfoils with a span of 120 mm grounded by means of a aluminum strip.

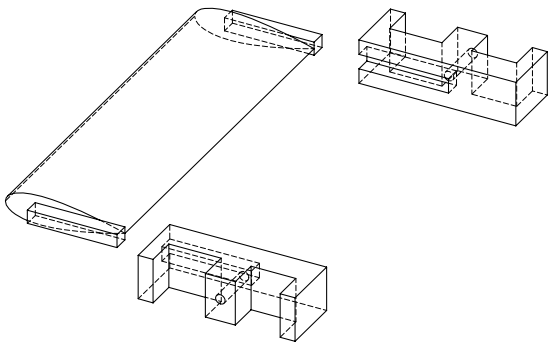

(a) Detail of the collector support system

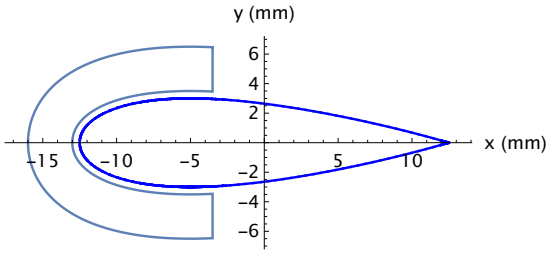

(b) Detail of the airfoil cap design for the C25T6 airfoil

Figure 3.6: Airfoil Collectors

The support system for the airfoils is designed to accommodate a wide range of chord sizes, from 25 mm to 100 mm. As depicted in Figure 3.6, the system consists of two supports

with rectangular slots, which are mounted onto the collector's base using a precision template to ensure accurate and discrete inter-collector spacings of 5 mm.

To secure the airfoils, they are slid into the rectangular slots, with each airfoil being fitted with two end caps that leave a 0.5 mm air gap to provide insulation from end effects. These end effects occur due to the intensified electric field at the ends of the airfoils, which can potentially lead to dangerous sparks. A more detailed analysis of the behavior of the end effects is provided in the following sections.

The grounding connections are realized by means of 5 wires that connect the airfoil grounding strips to a small support threaded in one of the four legs. A single copper wire then connects this support to the mains earth. This is to ensure that mechanical stresses won't affect the measurements.

3.1.3. Anode Base

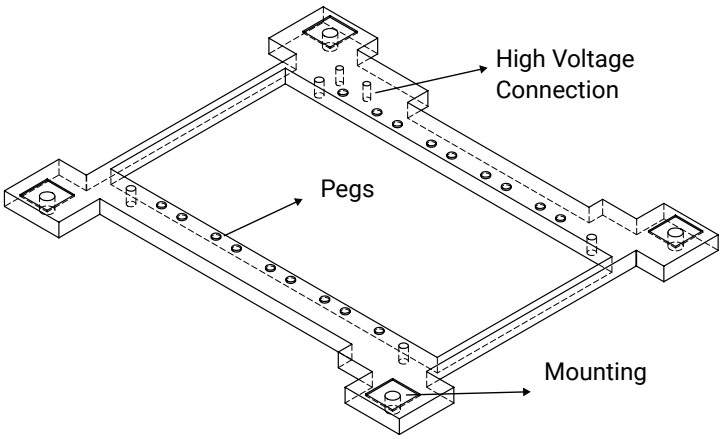

Figure 3.7: Detail of the Anode Base

The anode base serves as the housing for the wire emitters, which consist of 30 µm constantan wires that are tensed above the collectors. Custom-made pegs are used to regulate the inter-emitter spacing, and discrete variations of the gap can be achieved using the test rig. To prevent electrical losses and ensure operator safety, suitable insulating protections are employed to cover the ends of the emitters. Although not shown in the figure for clarity, these protections are an essential feature of the design.

The anode base is mounted at the top of the structural length and serves as the starting point for the high voltage connection. This connection is made using well-insulated cables that transmit the voltage from the power supply to the PMMA tower. A thin wire bridge is then responsible for the connection from the tower to the anode bases. This system

strikes an excellent balance between ensuring operator safety and using thin wires that do not affect the mechanical measurements.

3.2. Electrical Circuit

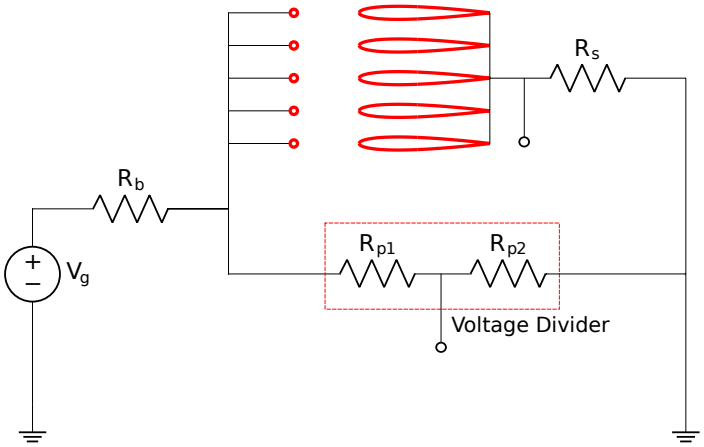

Figure 3.8: Electric circuit

Fig. 3.8 gives a detailed view of the electrical components and connections. A 0.996 MΩ ballast resistor R_b is connected at the output of the voltage supplier. The purpose of this resitor is of protection in the case of the appearance of sparks and of partially linearizing the $I - V$ characteristic of the circuit. The voltage drop across the ballast is in the order of 0.5 kV during nominal operation and increases only in the event of a malfunction.

A voltage divider, with total resistance of 152.9 MΩ and output resistance of 15.3 MΩ is connected in parallel with the thruster to measure the voltage between the electrodes. The input to output voltage is 1/1000 enabling safe probing of high voltages via an oscilloscope.

A shunt resistor of variable resistance, R_s, can be mounted to probe the current consumption waveform of the thruster. In particular, a 4 W 100 Ω resistor, which results in a good compromise between precision and safety, is used for measuring the current waveform during nominal operation and for investigation purposes. A low wattage 1.16 kΩ resistor is used to measure the onset voltage, which is associated with close-to-zero values of current.

3.3. Measurement Instrumentation

3.3.1. Power Supply

The required voltage is generated by the Glassmann PS/FC20R06 power supply which is capable of delivering up to 6 mA for a voltage which can vary from to 0 to 20 kV.

Figure 3.9: Glassmann PS/FC20R06 power supply

The power supply, shown in Figure 3.9, features precise control for the applied voltage and the maximum current along with an integrated ammeter and voltmeter. The ammeter was used to measure the total current supplied to the thruster and measurement instrumentation with a precision of 0.005 mA.

3.3.2. Signal Conditioner

Figure 3.10: Signal Conditioner

The purpose of using a signal conditioner is to amplify the signals generated by each load cell prior to them being transmitted to the oscilloscope. This particular signal conditioner, shown in Figure 3.10, is a custom-built instrument that was previously employed in other studies. The device comprises a front panel that houses a power switch and a display that is not utilized for this research. On the rear panel, there are four nine-pin input connectors, four BNC output connectors, and a GND/FLOAT switch that allows for the selection of whether to connect the instrument to the ground or not. Inside the casing, the electronics include linear potentiometers that enable the adjustment of zeros and gains for each input channel, which can be fine-tuned using a screw. The signal conditioner is

equipped with two different types of operational amplifiers, the OP37 and the MAX437. These amplifiers were chosen due to their ability to measure lift and drag in a wind tunnel, with the OP37 having a higher signal-to-noise ratio compared to the MAX437. Despite this difference, both amplifiers met the requirements for this thesis and were not replaced.

4 | Data processing

In this chapter, load and electrical measurements are described. The total thrust was directly measured by means of the 3 load cells. Electrical measurements of voltage and current were also performed to compute the required power.

4.1. Load Measurements

The structure is placed onto the load cell arrangement via the screw mechanism described in Section 3.1.1. The load cells measure the weight of the structure, which decreases when the thruster is turned on and generates an upwards force. The order of magnitude of the structure weight is 1.5 kg, and the order of magnitude of the thrust force is 5 g.

In order to compute the thrust a rigorous linearization procedure was employed. In principle, the output signal is a nonlinear function of the applied weight. This is not a function of the weight distribution since the mechanism introduced to precisely load the load cells transmits only point loads and no torques. The total load can be represented as the sum of the structure weight and a variable weight δW

$$s_{\text{on}} = f\left(W_{\text{tot}}\right) = f\left(W_{\text{struct}} + \delta W\right) \ . \tag{4.1}$$

The function can be linearized with a Taylor series expansion around W_{struct},

$$s_{\text{on}} = f\left(W_{\text{struct}}\right) + f'\left(W_{\text{struct}}\right) \ \delta W = s_{\text{off}} + k_{\text{sys}} \ \delta W \ , \tag{4.2}$$

where δW is a known weight, k_{sys} is the system calibration constant, and $s_{\text{on}}, s_{\text{off}}$ are the output signals when the thruster is respectively loaded and unloaded. Frequent and repeated measurements of the system calibration constant were taken during the entire experimental campaign by loading the structure with a small known weight of around 10 g, which was measured precisely using a precision scale available at DAER. Deviations from the mean value are in the order of 0.4%.

The effective thrust is computed by taking the difference $s_{\text{off}} - s_{\text{on}}$ between the load cell output signal when the thruster is switched off and on, and multiplying this value by the calibration constant of the system:

$$T_e = k_{\text{sys}} \left(s_{\text{off}} - s_{\text{on}} \right) . \tag{4.3}$$

Multiple measurements are taken to ensure repeatability and perform uncertainty estimation. Repeatability of the measurement is concerned with the estimation of the effect of the tension of the wires which carry the electrical current through the thruster. These wires can also transmit load and affect measurements, so to ensure a stationary tare, multiple measurements are taken. Uncertainty estimation is performed by computing the standard deviation from the mean of the multiple measurements and using a t-Student distribution to account for the low number of points to compute the 1σ uncertainty level.

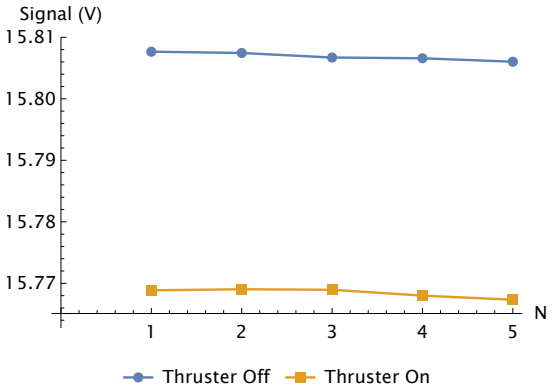

(a) Measurement history

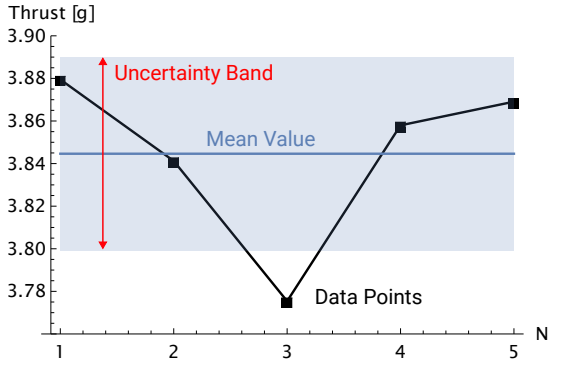

(b) Thrust force of each measurement, mean value and uncertainty band at the 1σ level

Figure 4.1: Example of the thrust measurement acquisition process for the C40T10S35SE configuration

Figure 4.1 shows an example of the measurement process. This method can help reducing the overall uncertainty below 0.05 g.

All measurements are referenced to a single cell and reported in dimensionless formulation by scaling with the reference value $T_{\text{ref}} = \epsilon_0 V_a^2 / d$ and the span b,

$$C_{Te} = \frac{T_e}{5 \; T_{\text{ref}} \; b} . \tag{4.4}$$

4.2. Electrical Measurements

The measurement of electrical quantities was performed in order to compute the total power consumption and derived performance indicators. The reference circuit model is described in Figure 3.8. The voltage between the electrodes was measured using the voltage divider which was in parallel with the system.

$$V_c = \frac{R_{\mathrm{d,tot}}}{R_p} V_m \ , \tag{4.5}$$

where V_c is the voltage drop across the entire voltage divider, V_m is the measured voltage, $R_{\mathrm{d,tot}} = R_{\mathrm{p1}} + R_{\mathrm{p2}}$ is the total resistance in parallel with the thruster and R_p is the equivalent parallel resistance between the output resistance of the divider, R_{p2}, and the oscilloscope input impedance, z_{in}. The latter is equal to 1 MΩ.

$$R_p = \frac{R_{\mathrm{p2}}\ z_{\mathrm{in}}}{R_{\mathrm{p2}} + z_{\mathrm{in}}} \ . \tag{4.6}$$

It is worthwhile to note that the voltage divider gain is 1/1000 but, because of the addition of a low impedance scope measurement system, the actual ratio is 6.77/1000. The thruster current consumption can be recovered by subtracting the current flowing through the measurement unit from the total current, measured with the power supply ammeter,

$$I_c = I_{\mathrm{tot}} - \frac{V_c}{R_{\mathrm{d,tot}}} \ . \tag{4.7}$$

The thruster power consumption can therefore be computed multiplying the current and the voltage $P = V_c I_c$. Similarly to the thrust measurements, the power consumption is made dimensionless and referenced to a single unit:

$$C_P = \frac{P}{5\ P_{\mathrm{ref}}\ b} \ . \tag{4.8}$$

4.2.1. Uncertainties

All measurement uncertainties are assumed uncorrelated and with symmetrical distribution, hence the RSS (Root-Square-Sum) method can be used to compute propagation of errors, starting from the general form described by previos equations:

$$w_Y^2 = \sum_{i=1}^{n} \left(\frac{\partial Y}{\partial x_i} \right)^2 w_{x_i}^2 \tag{4.9}$$

where w_Y is the measurement uncertainty of Y, $\frac{\partial Y}{\partial x_i}$ is the sensitivity of Y to variation of the i-th variable x_i, and w_{x_i} is the measurement uncertainty of x_i.

4.2.2. Inception Voltage

The inception voltage is a crucial parameter that plays a significant role in the dimensionless model presented in Chapter 2. It represents the voltage at which the first streamer discharge is observed, and a non-zero current, usually in the order of magnitude of 0.1 µA, can be measured. The inception voltage is an important parameter to consider since it characterizes the voltage range where the thruster starts generating thrust. Moreover, it can provide useful information on the onset of the electrical breakdown process in the thruster, which is a crucial phenomenon to understand for the proper functioning of the device.

The inception voltage is typically measured by gradually increasing the voltage applied to the thruster and monitoring the current response until a non-zero current is detected. However, background noise generated by the measurement system can introduce uncertainty to the measurement. To account for this uncertainty, the non-zero current is defined as the mean value greater than three times the root-mean-square (rms) noise signal, known as the "3σ criterion". In other words, the measured current must be greater than three times the standard deviation of the background noise in order to be considered a valid signal for determining the inception voltage.

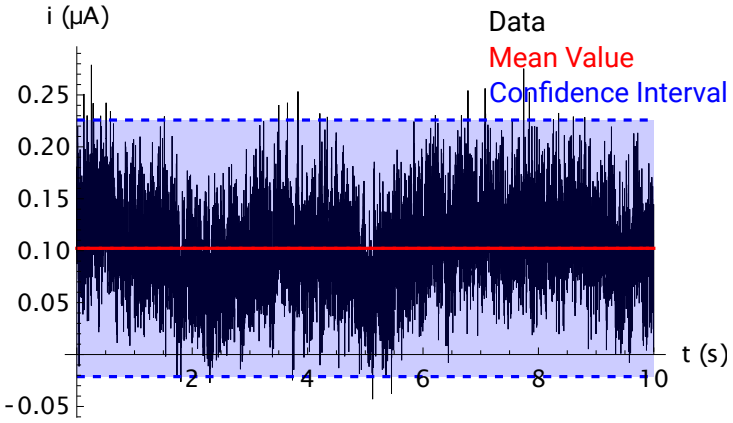

Figure 4.2: Inception voltage measurement for the C25T6S35SE configuration, the confidence interval corresponds to the $\pm 3\sigma$ band

Figure 4.2 shows an example of such measurement which was performed by inserting a 1.10 kΩ shunt resistor R_s as in Fig. 3.8. Preliminary tests show that this method ensures an uncertainty in the order of 200 V.

4.3. Measurement Acquisition

Data from the analog output of the load cells, voltage divider, and shunt resistor were acquired by an oscilloscope. The choice of parameters such as time window and sampling frequency depends on the instrumentation from which the output is generated.

During the tests involving thrust measurement, the output signal for each load cell was received from the signal conditioner to the oscilloscope. The time window was set to 2 s, while the sampling frequency was equal to 50 kHz for each acquisition. These values were selected based on the fact that the overall force applied to the load cells corresponds to the sum of three contributions: a stationary signal (which is equal to the structure weight and thrust), a high-frequency noise, and a low-frequency parasitic weight signal (which is due to the structural relaxation process of the wires and other members). By taking multiple acquisitions of a short time frame and adopting statistical post-processing of the data, it was possible to eliminate the high-frequency noise and check that the low-frequency parasitic signals are negligible. The oscilloscope was set in hi-res mode to increase the resolution from three to four significant digits and limit the quantization error.

5 | Results

This chapter discusses the results of the experimental campaign.

5.1. Current Waveform Measurement

This section presents the findings concerning the thruster's current consumption waveform in time and frequency domain. To obtain these results, the scope sampling frequency was set to 1 GHz and a thruster off acquisition was performed to ensure that no significant disturbance is present below 100 MHz (radio frequency range). The C25T6S35 configuration was used to perform this study.

An acquisition was made without the protection caps to study the end effects.

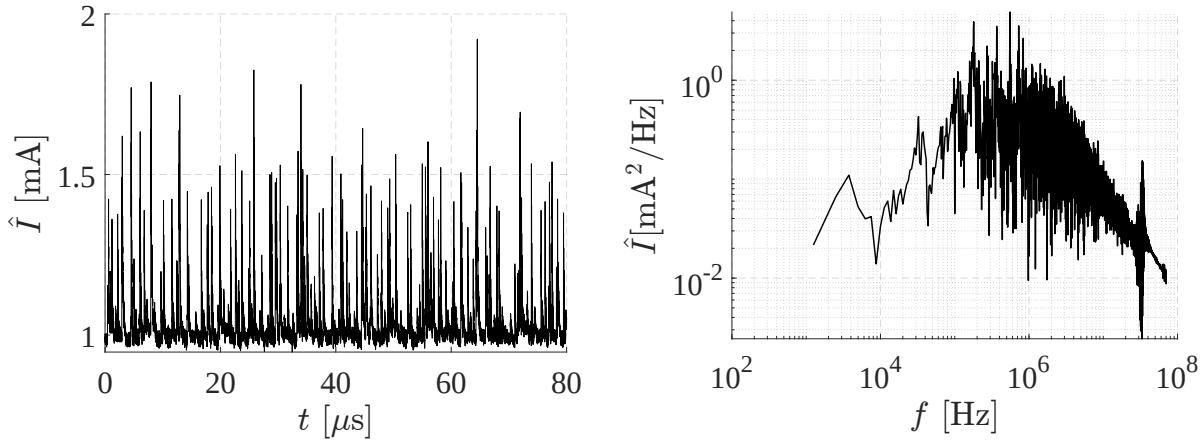

(a) Current

(b) Power Spectral Density

Figure 5.1: Current in time and frequency domain for the C25T6S35 configuration with no end effect protection

Figure 5.1 shows the current waveform in time and frequency domain for the studied configuration. It is possible to see that, the current is the superposition of a mean value (in the order of 1 mA) and peaks with an amplitude comparable to the mean value. These peaks are associated with breakdown streamers occurring at the airfoil ends. These are

not physical and are caused by the fact that the grounding strip was cut and glued to the airfoil leaving the sharp edges unprotected. The sharp edges, even though the potential is 0 V, intensify the local electric field at the cathode. This can give rise to a plethora of parasitic phenomena which increase the current consumption and favour the formation of streamer discharges. These discharges have an audible component (as demonstrated by the PSD in Figure 5.1b) and a high frequency component. The increase in current can be explained by the ignition of a second corona discharge at the cathode as hypotesized by Barret et al. [22].

To limit the effect of the airfoil ends a range of solutions was tested. Initially, a few layers of high end self rubbing tape carefully applied at the two ends (with an electrical rigidity of 40 kV/mm and higher) were used. The results are shown in the following figure

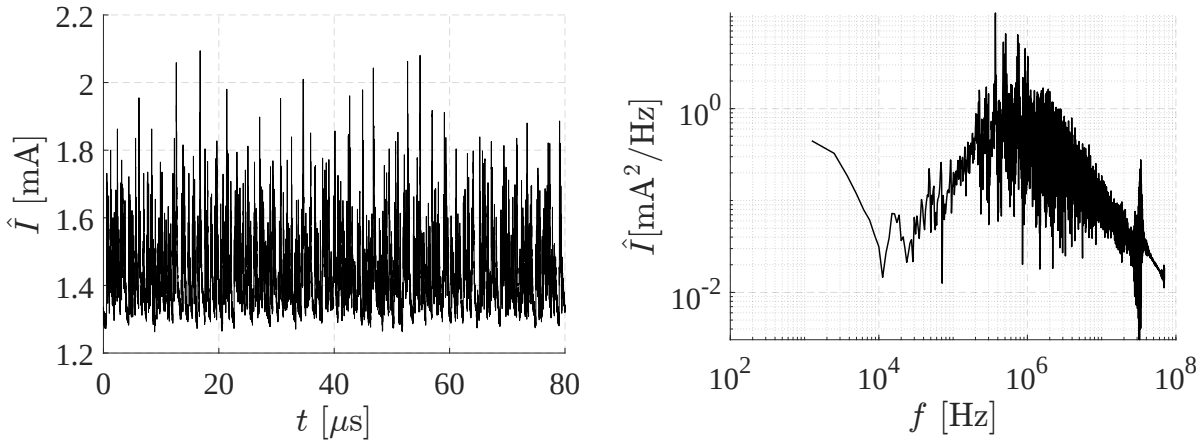

(a) Current

(b) Power Spectral Density

Figure 5.2: Current in temporal and frequency domain for the C25T6S35 configuration with self-rubbing tape as protection

As it is possible to see from Figure 5.2, the performance is worsened since breakdown streamers and inverse corona are amplified. It is hypothesized that this is due to the fact that insulating materials do not change the electric field distribution which is still able to ionize the air present in air pockets below the self rubbing tape and the formation of anode-directed luminous streamers was observed.

For this reason custom PLA caps were designed and printed for each airfoil in the parameter space. The caps are mounted at the airfoil end so that they leave a 0.5 mm air gap allowing space charges to move freely but, because of their design, the formation of ionized channels is discouraged. This is due to the fact that this channel would be too long; thus requiring too much power to be maintained [19].

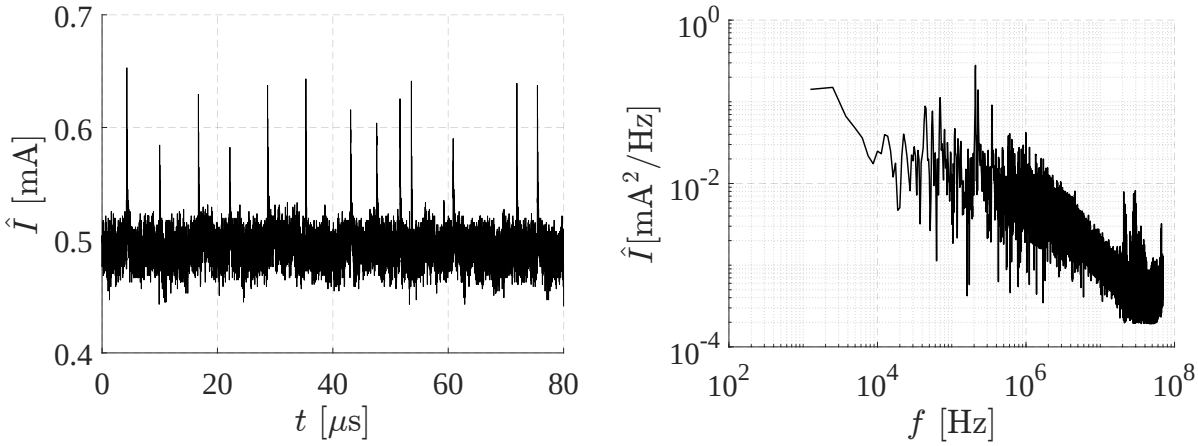

(a) Current (b) Power Spectral Density

Figure 5.3: Current in temporal and frequency domain for the C25T6S35 configuration with PLA caps as protection

Figure 5.3 shows that the current, in this configuration is half of the value reached by unprotected airfoils and is repeatable. High frequency unstable discharges are still present but the magnitude is reduced and the spectral power has lost at least on order of magnitude across the entire frequency range.

5.2. Chord and Thickness dependence

In this section, the effect of the chord and of the thickness on the performance of the thruster is presented. The evaluation is done in the standard conditions (1.8). Figure 5.4 shows the behaviour of the effective thrust, power and effective thrust to power coefficients for the different airfoils investigated as a function of the thickness.

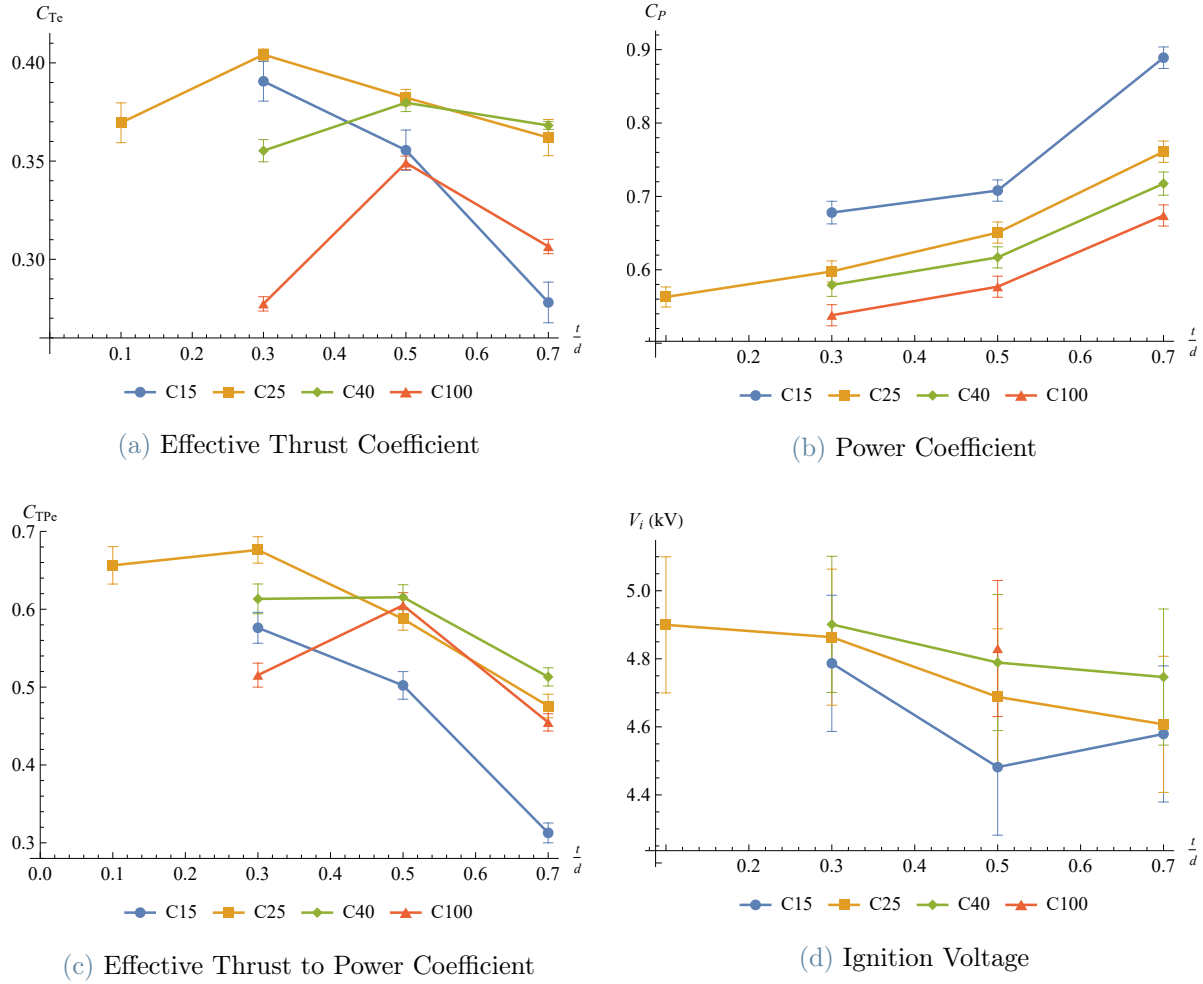

(a) Effective Thrust Coefficient

(b) Power Coefficient

(c) Effective Thrust to Power Coefficient

(d) Ignition Voltage

Figure 5.4: Evaluation of the performance indicators, for each chord, as a function of t/d ($d = 20\,\text{mm}$).

The behaviour of C_{Te}, shown in Figure 5.4a, is influenced by electrical and aerodynamic parameters. On one hand, increasing the thickness has a beneficial effect on the generated electrical thrust since the discharge section increases [1]. On the other hand, an increase in the thickness increases the t/c ratio which makes the airfoil less aerodynamic; moreover, it decreases the S/t parameter causing a worsening of the aerodynamic performance due to blockage effects [1]. The combination of these effects results in the presence of a local maximum as function of thickness for a given chord. Both the C100 and C40 families present this maximum in the corresponding T10 airfoil while the T14 airfoil suffers from blockage effects. The C25 family presents this maximum in the T6 airfoil since the C25T10 airfoil has a shape with poor aerodynamics. The local maximum for the C15 chord family should presumably appear on the left, outside the investigated parameter space.

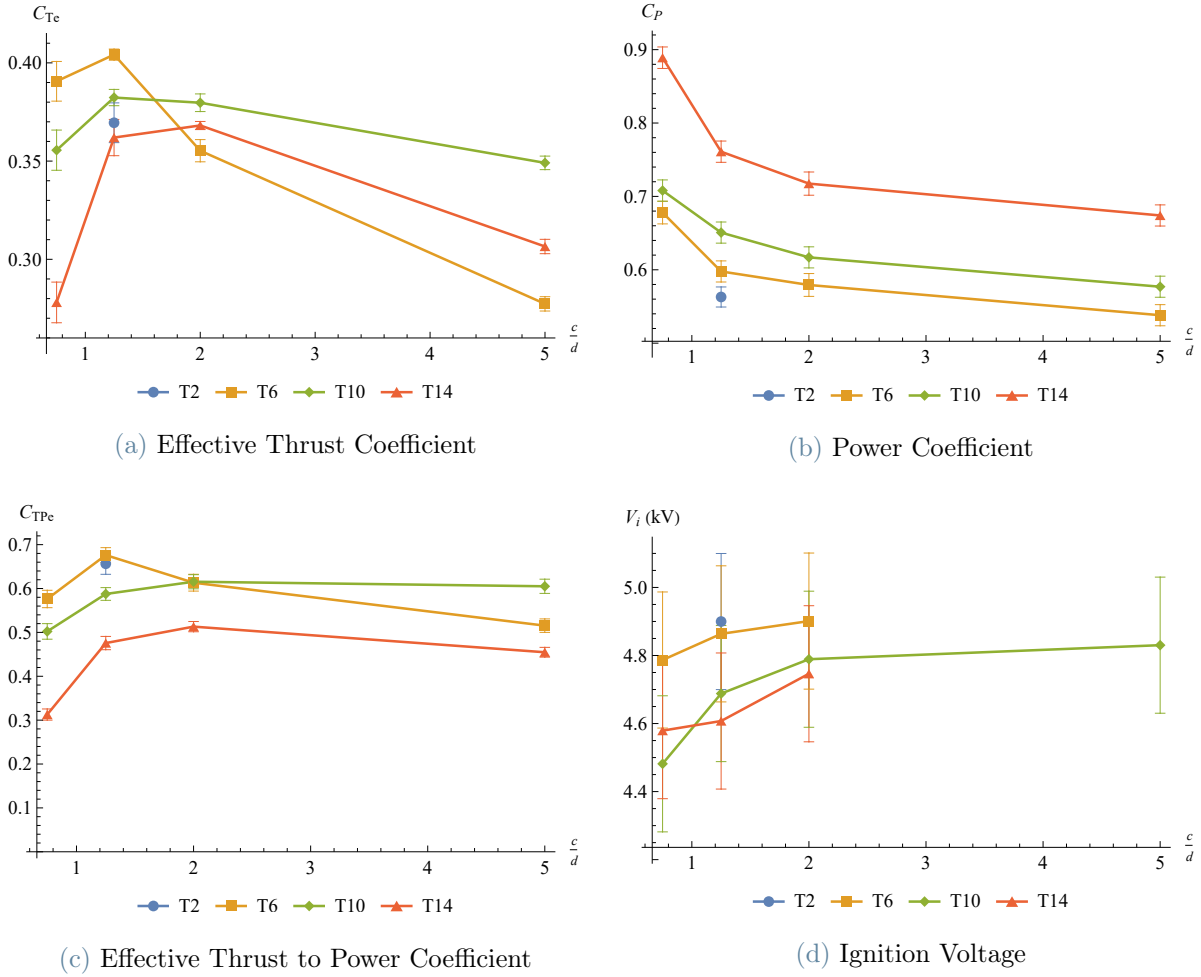

(a) Effective Thrust Coefficient

(b) Power Coefficient

(c) Effective Thrust to Power Coefficient

(d) Ignition Voltage

Figure 5.5: Evaluation of the performance indicators, for each thickness, as a function of c/d ($d = 20\,\text{mm}$).

Figure 5.5 shows the behaviour of the performance parameters for each thickness and variable chord. It is possible to see that decreasing the chord with respect to well-known 100 mm case [1, 2, 32] is generally beneficial. Indeed, the thrust coefficient always admits a local maximum whereas the power coefficient increases. This means that the thrust to power has a local maximum.

This is because a reduction of the chord decreases the weight of the drag in the effective thrust coefficient $C_{Te} = C_T - \frac{1}{2}(c/d)C_D$, after Equation (**??**). This is possible until the t/c parameter becomes too large, leading to a bluff airfoil which favours flow separation and the related drag increase.

Overall, the global maximum for C_{Te} in the parameter space is represented by the C25T6 airfoil. It remains unclear whether the C15T2 airfoil, not present in this parameter space

because of manufacturing issues, could have a higher thrust. However, the investigated trends indicate that smaller and thinner airfoils could presumably increase the effective thrust in the order of 15 %.

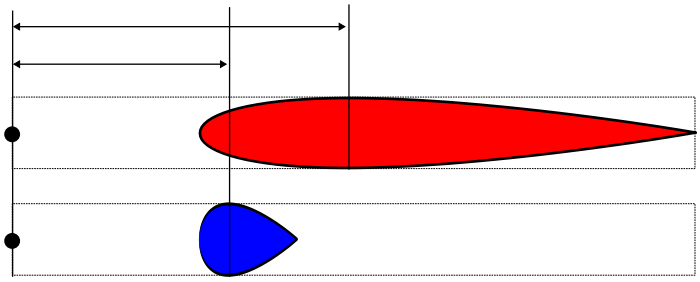

Figure 5.6: Distance between emitter and maximum thickness section of the airfoil for two collectors of different chord and equal thickness

The power coefficient, being less influenced by aerodynamics, shows a simpler behaviour. Similarly to the thrust coefficient, increasing the thickness produces an increase of the power coefficient because also the discharge section grows. Decreasing the chord also increases the power coefficient. This is probably due to the fact that a decrease in the chord has the effect of compressing the airfoil shape closer to the emitter, as shown in Figure 5.6. This flattens the leading edge and moves the section with maximum thickness closer to the emitter, leading to an increase in current consumption.

As for thrust to power, C_{TPe} shows the combination of every effect mentioned so far. It is interesting to observe that, as the chord is decreased, there is a slight increase of C_{TPe} followed by a decrease. This indicates that a further extension of the parameter space by reducing chord and thickness, although beneficial for the total trust, would not necessarily improve C_{TPe}.

It is worth noting that in Figure5.4 the dimensionless coefficients trends correspond to the dimensional trends. In fact, as presented in tables 2.1 and 2.2, each dimensional quantity can be written as the product of the relevant coefficient and reference factor, as for instance $T_e = C_{Te}T_{ref}$, and in the data above the reference factors are constant, given the experiment conditions. Instead, other results in the followings, as the ones about the gap effects, include also combined variations of coefficients and reference factors.

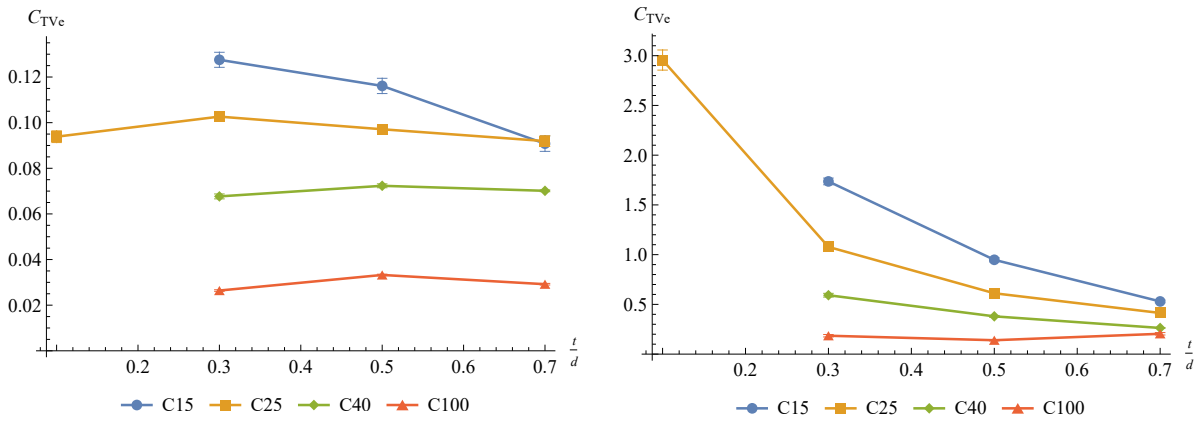

(a) Cell Volume, C_{TVe}

(b) Airfoil Volume, C_{TVe}

Figure 5.7: Effective Volumetric Thrust coefficient behaviour based on the cell volume and collector volume

Figure 5.7 shows the behaviour of the Effective Volumetric Thrust Coefficient as function of the collector thickness. In Figure 5.7a the reference volume is the one of a thruster unit $S\,(d+c)\,b$ and is an indicator of the spatial size of a single unit or cell; this indicator can be useful in studying the benefits of a multiple units configuration. In Figure 5.7b the reference volume $(t\,c\,b)$ is proportional to the volume of a collector, and it is an indicator of the mass of the airfoil, if the collector is fully filled. Both these coefficients suggest that moving towards shorter and thinner collectors is beneficial.

The most important design parameters available for an optimization process are C_{TAe}, C_{TVe} and C_{TPe}. A local optimization must account for the weight assigned to each performance indicator and consider structural and manufacturing parameters. It is however clear that airfoils with large chords are inefficient and a reduction is suggested. In this work, the C25 family is identified as the global optimum since it results in an acceptable trade-off between the above parameters.

5.3. Spacing variation

The dependence on the spacing between units has already been studied by several authors [1, 9, 21]. In particular, a study on the C100 family [1] found that reducing the spacing between units results in a trade-off between the total thrust generated, which decreases by aerodynamic blockage as the spacing diminishes, and the surface thrust density, which presents a local maximum. Another work [21] showed that lowering the emitter spacing (i.e. increasing the emitter density) is not always beneficial because of the electrostatic in-

teraction between close wires. This is known as *shielding*, as it limits the corona inception of closely packed wires.

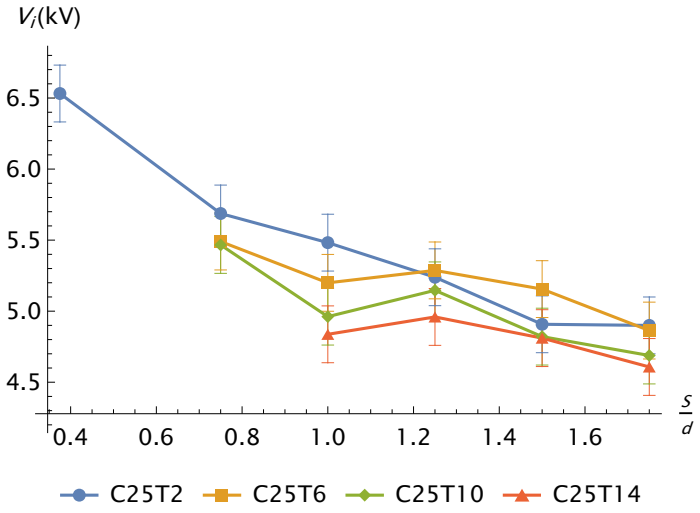

Figure 5.8: Ignition Voltage as a function of S/d ($d = 20\,\text{mm}$).

Figure 5.8 shows the behaviour of the ignition voltage as function of the spacing between C25 airfoils under the standard conditions (1.8). The differences between airfoils of different thicknesses are not clearly measurable since they fall within experimental errors. It is however evident that decreasing the spacing favours the electrostatic interaction between the emitters, and this results in an increase of the ignition voltage.

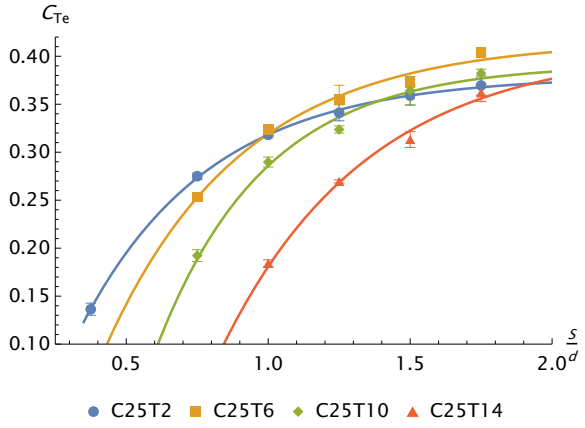

(a) Effective Thrust Coefficient

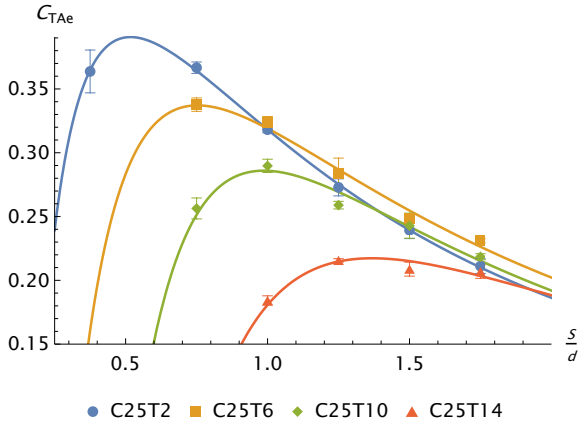

(b) Power Coefficient

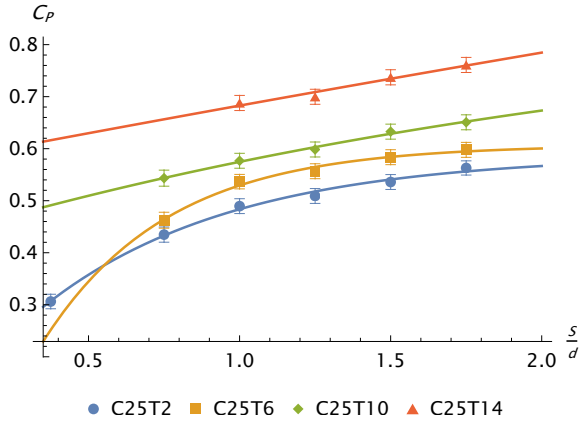

(c) Effective Surface Thrust Density Coefficient

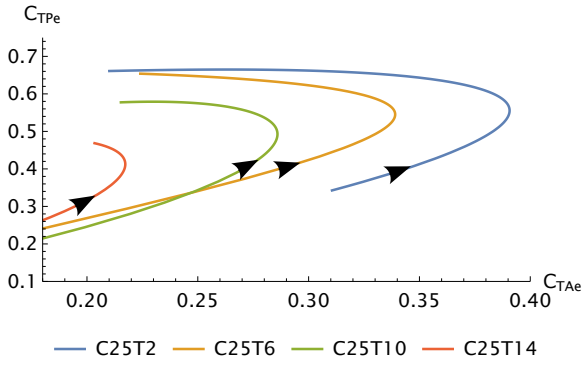

(d) C_{TAe}-C_{TPe} curves, arrows indicate the direction of increasing spacing

Figure 5.9: Influence of the inter-collector spacing on the thruster performance for a SE configuration

Figure 5.9 shows the behaviour of all the performance parameters versus the spacing, for thrusters with one emitter per collector (SE configuration) as in the previously presented results. The plots of C_{Te} and C_P show the experimental data points as well as the relevant fits, already introduced in a previous work [1]:

$$\begin{cases} \dfrac{T}{b} = k_1 \left(1 - k_2 e^{-k_3 s}\right) \\ \dfrac{P}{b} = k_4 \left(1 - k_5 e^{-k_6 s}\right) \end{cases} . \tag{5.1}$$

The fits for C_{TAe} and C_{TPe} are derived from the previous ones. Figure 5.9a shows that C_{Te} decreases as the spacing is reduced. This effect is believed to be a combination of both

the aerodynamic blockage and the electrostatic shielding, progressively important as the spacing decreases. The power coefficient shows a similar behaviour but the exponential trend is less visible. This is because the power is less influenced by aerodynamics than by the electrostatic interaction, which is more important at small spacings.

C_{TAe} increases as the spacing is decreased but reaches a local maximum, then it drops following the effective thrust. The C25T2 airfoil reaches the highest effective thrust density C_{TAe} because aerodynamic losses become important only at very low spacings, given the fact that the airfoil (NACA0008) has a low t/c and hence a favourable slender shape.

Overall, Figure 5.9d shows that a global maximum, in the considered space, is found for the C25T2 airfoil which maximises the effective thrust density coefficient given a desired effective thrust to power and viceversa.

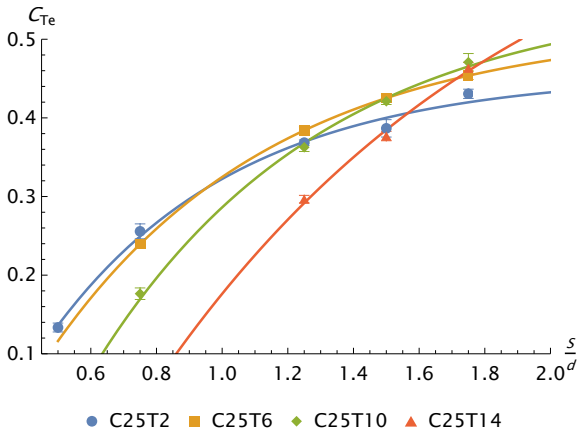

(a) Effective Thrust Coefficient

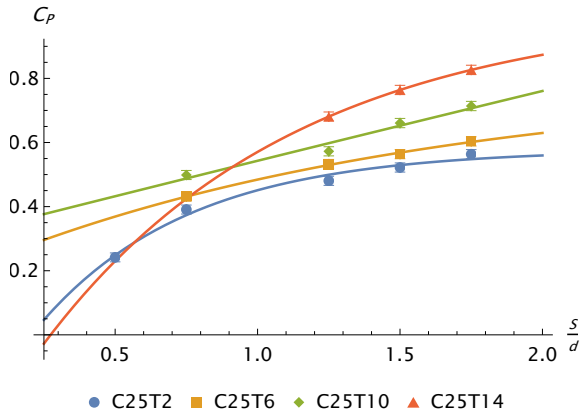

(b) Power Coefficient

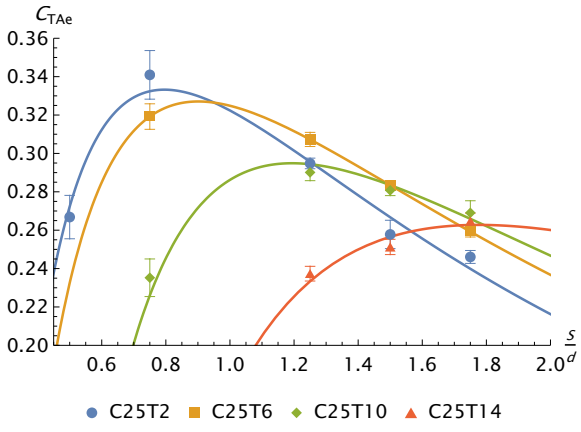

(c) Effective Surface Thrust Density Coefficient

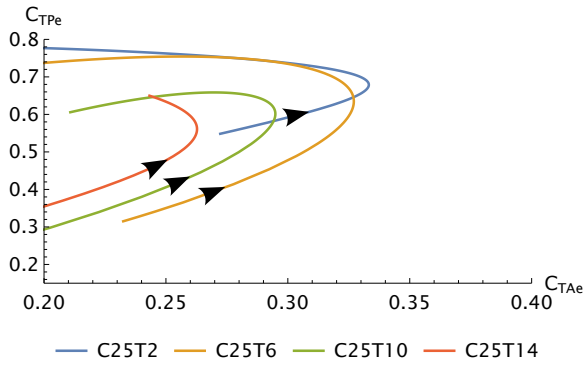

(d) C_{TAe}-C_{TPe} curves, arrows indicate the direction of increasing spacing

Figure 5.10: Influence of the inter-collector spacing on the thruster performance for a DE configuration.

Figure 5.10 shows the same analysis, repeated for the C25 family in a double emitter (DE) periodic configuration. In this case the spacing is S between collectors and $S/2$ between emitters, as in Figure 1.15b. It is possible to see that at large spacings, a DE configuration boosts the generated thrust keeping the same power consumption, a behaviour already evidenced in [2].

Again, it is possible to fit with an exponential behaviour both the effective thrust and the power consumption. The effective thrust density admits a local maximum, reached by the C25T2 configuration, but the value is smaller than for the SE configuration. In fact, a DE configuration becomes unfavourable at low spacings because the double number of emitters may more easily cause the shielding phenomenon [21]. Accordingly, there is a performance drop for the C25T2 airfoil even if it is thin and aerodynamically capable of working at low spacing.

The curves in Figure 5.10d show that C25T2 still exceeds C25T6 in the DE case, although the differences are small, and at large spacings the two airfoils have a similar C_{TPe}.

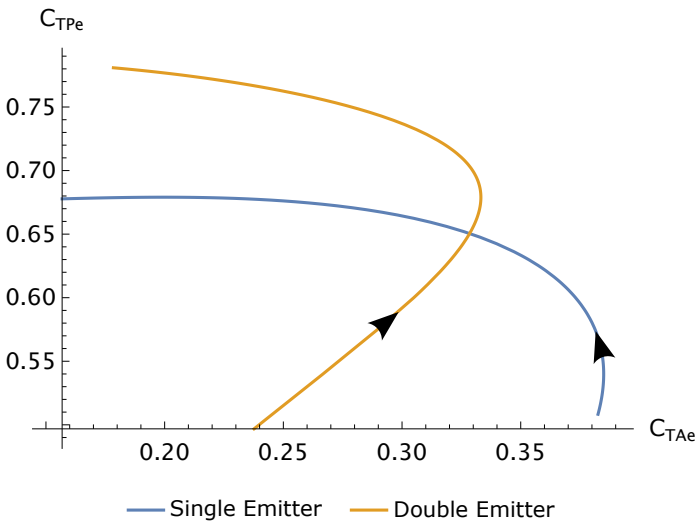

Figure 5.11: C25T2 performance in SE and DE configuration; the arrows indicate increasing spacings

Further details about the C25T2 are presented in Figure 5.11, which compares its SE and DE performance curves. It is seen that the DE configuration maximizes the thrust to power at high spacings while the SE configuration maximizes the surface thrust density at low spacings.

5.4. Gap and voltage characterization

A variation of the gap d will cause a variation of all the dimensionless parameters introduced in Chapter 2 since d is chosen as scaling factor for all the lengths; for this reason, a detailed study of the gap influence can assess the capability of the dimensionless parameters to describe the underlying physics. The analysis include voltage variations, since d and V_a contribute to determine the electric field. The C25T6 airfoil, which maximises C_{Te} for a 20 mm gap, was chosen for this investigation. The measures are performed in the nominal corona regime, before the onset of breakdown which occurs at lower voltages when the gap is reduced. The investigation spans a range of gaps $10 \leq d \leq 30$ mm and a range of voltages $3 \leq V_a \leq 20$ kV.

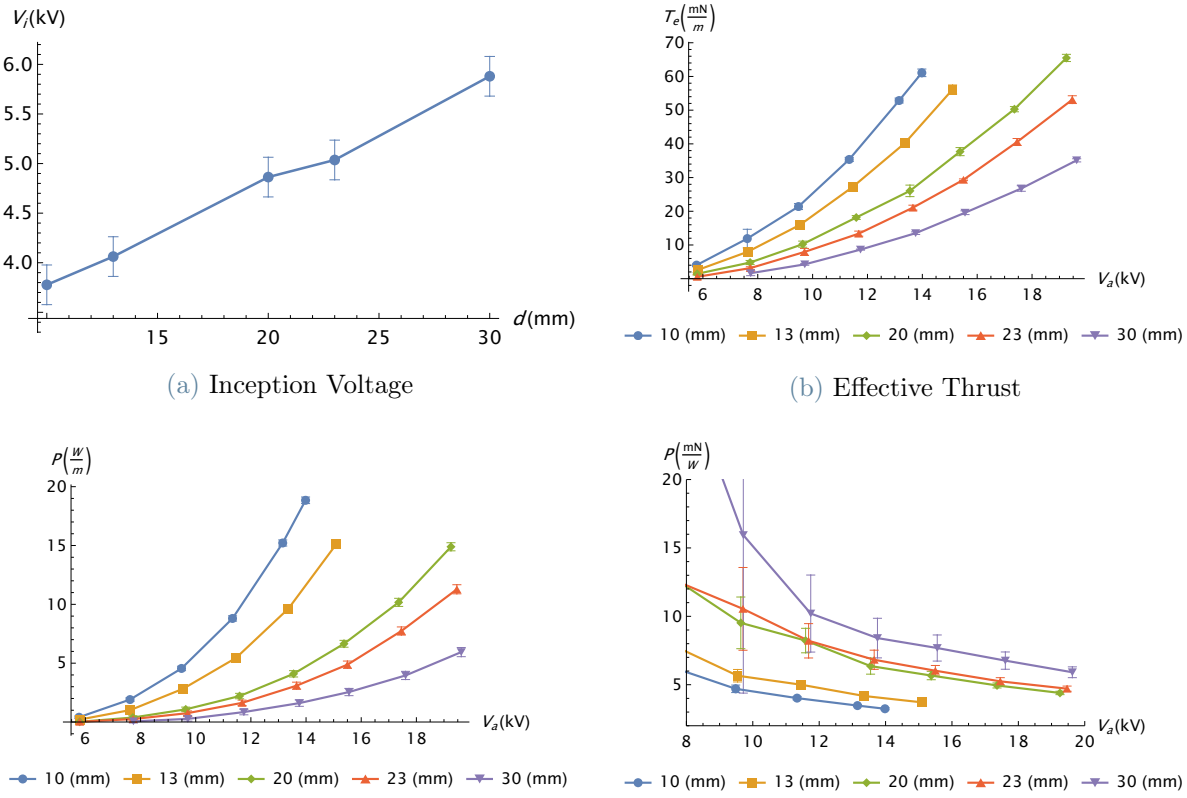

(a) Inception Voltage

(b) Effective Thrust

(c) Power

(d) Effective Thrust to Power

Figure 5.12: Influence of the voltage and gap variation on the dimensional performance indicators

Figure 5.12 shows the variation of the dimensional parameters with respect to the gap and the applied voltage for the C25T6S35 single emitter configuration. The ignition voltage, depicted in Figure 5.12a, increases as the gap is increased, with an apparently obvious

trend. However it is noteworthy that this phenomenon is related to what is shown in Figure 5.8, where a decrease in spacing S results in an increase of the ignition voltage V_i: in fact, according to the scaling introduced in §2, the dimensionless spacing is S/d, so an increase in the gap should give similar effects to a reduction of the spacing, i.e. a gap increase with constant inter-emitter spacing and an emitter spacing reduction at constant gap should have similar physical effects. This is indeed confirmed by comparing Figure 5.8 and 5.12a.

The other dimensional parameters exhibit a behaviour consistent with the scaling of §2: for instance, the effective thrust is $T_e = C_{Te}\ T_{ref} = C_{Te}\ \epsilon_0 V_a^2/d$, and Figure 5.12b shows that T_e mainly follows the reference factor V_a^2/d, growing with V_a^2 and decreasing as the gap is increased. Also the power follows its reference factor V_a^3/d^2 and varies inversely with the gap; accordingly, the effective thrust to power ratio exhibits the opposite behaviour, scaling as d/V_a. The latter is not easy to determine at low voltages since it is defined as the ratio of two quantities that tend to zero as the applied voltage decreases, and correspondingly the error bars are inherently emphasized.

In general, the trends in Figure 5.12 do not indicate that C_{Te}, C_P, C_{TPe} are constant, however their trends are masked by the reference factors, and need a separate analysis.

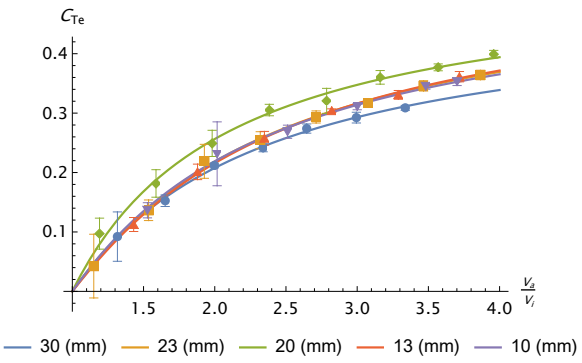

(a) Effective Thrust Coefficient

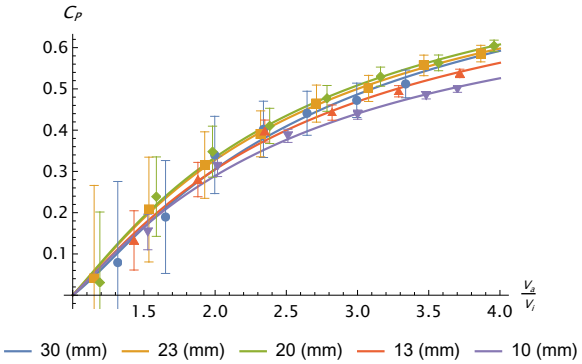

(b) Power Coefficient

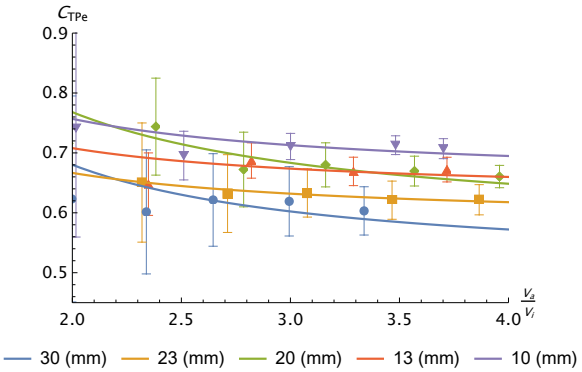

(c) Effective Thrust to Power Coefficient

Figure 5.13: Influence of gap and voltage variations on the behaviour of the dimensionless coefficients

For the same data of Figure 5.12, the behaviour of the dimensionless coefficients as a function of *scaled voltage* and gap are presented in Figure 5.13. The use of the scaled voltage V_a/V_i automatically includes the influence of the ignition voltage. In this case, the discrete points represent experimental data while the solid lines are modelling functions. For both the effective thrust and power coefficient the following expansion is adopted:

$$f\left(\frac{V_a}{V_i}\right) = c_0 + c_1\left(\frac{V_a}{V_i}\right)^{-1} + c_2\left(\frac{V_a}{V_i}\right)^{-2}. \tag{5.2}$$

The series is truncated at order 2 in order to avoid over-fitting. The coefficients can depend on d, and a constraint $c_0 + c_1 + c_2 = 0$ is imposed in order to ensure that when the scaled voltage is 1 no thrust is generated ($V_a = V_i$ condition or low voltage limit). Under the opposite condition $V_a \gg V_i$ (high voltage limit) the functions inherently tend to constant values.

The trends of the coefficients C_{Te}, C_P, C_{TPe} can now be analyzed in detail. The effective

thrust coefficient, as the gap is decreased, shows an initial increase and then a decrease indicating $d = 20\,\text{mm}$ as a local maximum. On one hand, decreasing the gap increases both t/d and S/d which are beneficial, up to a certain extent, to C_{Te}. On the other hand, the c/d parameter, which represents the weight of the drag coefficient in $C_{Te} = C_T - \frac{1}{2}(c/d)C_D$, also increases. This opposite behaviour explains the presence of a local maximum.

The power coefficient dependency on the gap exhibits the same local maximum found in C_{Te} with the difference that the variations around this maximum are smaller, especially at high gaps. The explanation for this trend is, once more, due to opposite behaviour of the geometrical dimensionless parameters: increasing t/d and S/d increases the power coefficient, whereas increasing c/d reduces it.

The model for the effective thrust to power coefficient C_{TPe} was assumed to be the ratio of the fitting functions for C_{Te} and C_P. In 2.3, using a simple 1D formulation without aerodynamic drag, it is shown that C_{TP} is a constant. As a comparison, in Figure 5.13b data points tend to a constant trend at high scaled voltages, consistently with Equation (5.2). However, at low voltages, the fits ratio becomes less reliable because both the effective thrust and the power coefficient tend to zero. As regards to the dependence on the gap, when d increases C_{TPe} decreases, indicating a trend that is opposite to the dimensional value.

5.5. Effect of the Grounding Strip Length

The grounding strip length is an important geometrical parameter for the performance of the thruster. Its effect is not discussed in the present literature; Barret et al. used airfoils with an unspecified grounding strip length [32], Komich et al. used metal sheets [16] and all previous works grounded the 45% of the cathode surface [1, 2]. It is possible to hypothesize that, for airfoils with a large chord, the difference between partially and fully grounded airfoils is negligible due to the fact that the extent of the metal surface is larger than the distance required for ions to be neutralized by surface processes. It is however unclear if this effect still holds for shorter cathodes and if there is a dimensionless parameter which governs this phenomenon.

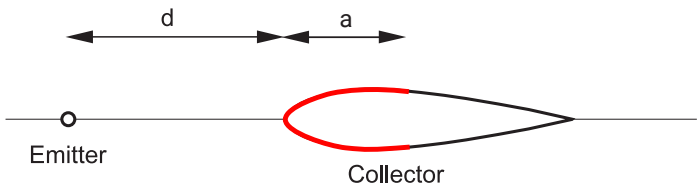

Figure 5.14: Ground Strip (in red) over an airfoil. The parameter a represents the x-axis length of the strip.

To perform this evaluation, the T10 airfoils of each chord family were studied in the standard configuration (1.8) at a variable grounding strip length which corresponds to 45%, 80% and 100% of the airfoil chord. To evaluate the result, the a/d dimensionless parameter was used

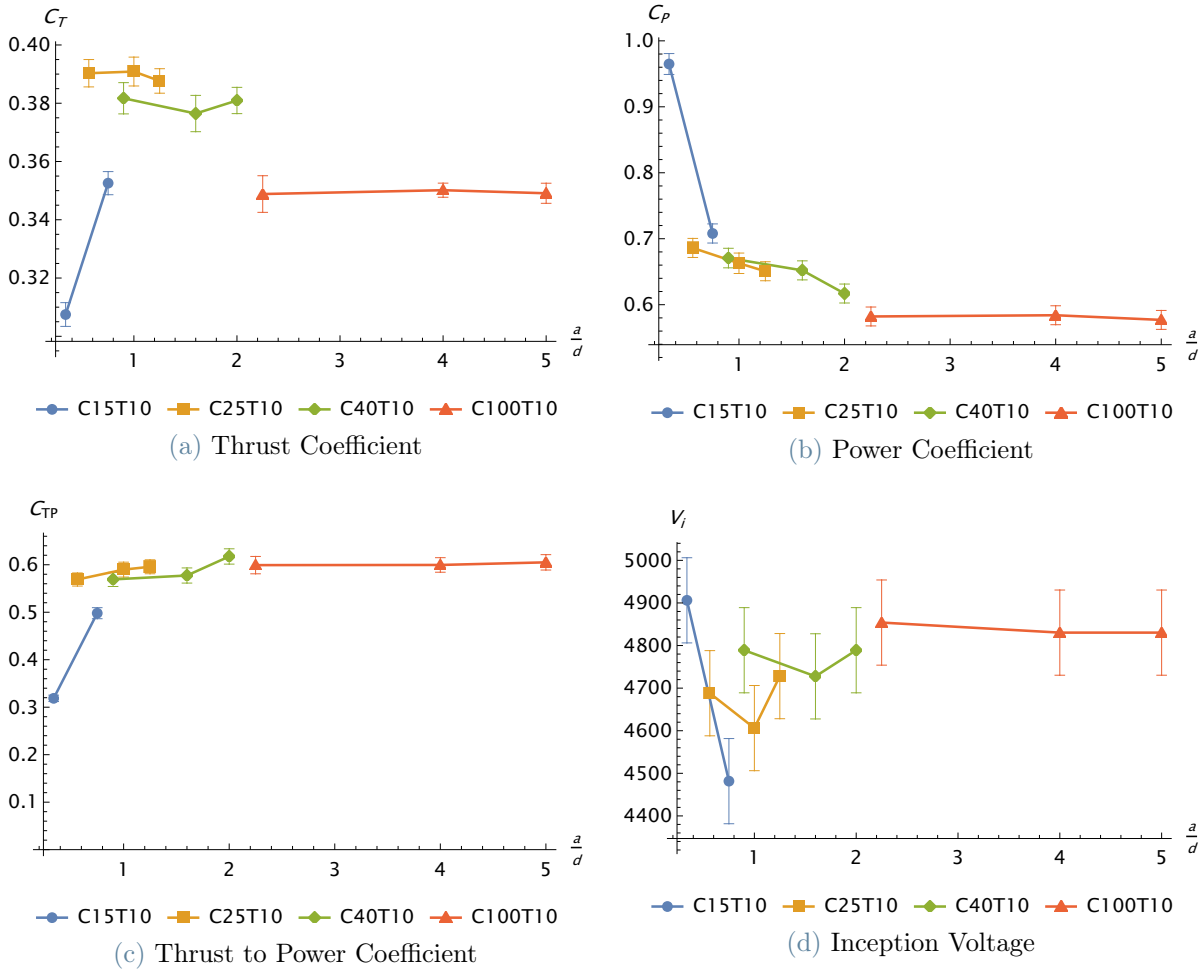

(a) Thrust Coefficient

(b) Power Coefficient

(c) Thrust to Power Coefficient

(d) Inception Voltage

Figure 5.15: Performance indicators for the T10 airfoils as a function of the a/d dimensionless parameter

Figure 5.15 shows the behaviour of the main performance parameters as the length of the grounding strip is changed. It is possible to see that the inception voltage, except for the C15T10 airfoil, doesn't experience large variations indicating that the length of the conductive strip is not relevant for the inception of corona discharges. The thrust coefficient, expect for the C15T10, airfoil is also not affected by the dimensionless parameter's variations and it is hypothesized that, relative differences, are, if present, within the current uncertainty level.

The power coefficient shows an interesting trend. It is possible to see that increasing the a/d parameter will cause a decrease in the electrical power consumption. This indicates that the behaviour of the power coefficient is actually controlled by the a/d parameter rather than the c/d. The explanation behind these variations is complementary to the one given in Chapter 5.2.

Finally, the thrust to power coefficient shows the combined effect of the two previously mentioned parameters indicating that a fully grounding airfoil with a smaller chord is more efficient than an equivalent partially grounded airfoil.

5.6. Emitter Degradation

The emitter degradation is a crucial topic for any future application of this technology. The goal of this section is not rigorously evaluate the performance of the emitter as a function of time but to show what the emitting surface looks like and evaluate its changes during the tests. All images were captured with Hitachi TM3000 electronic microscope available at DAER laboratory.

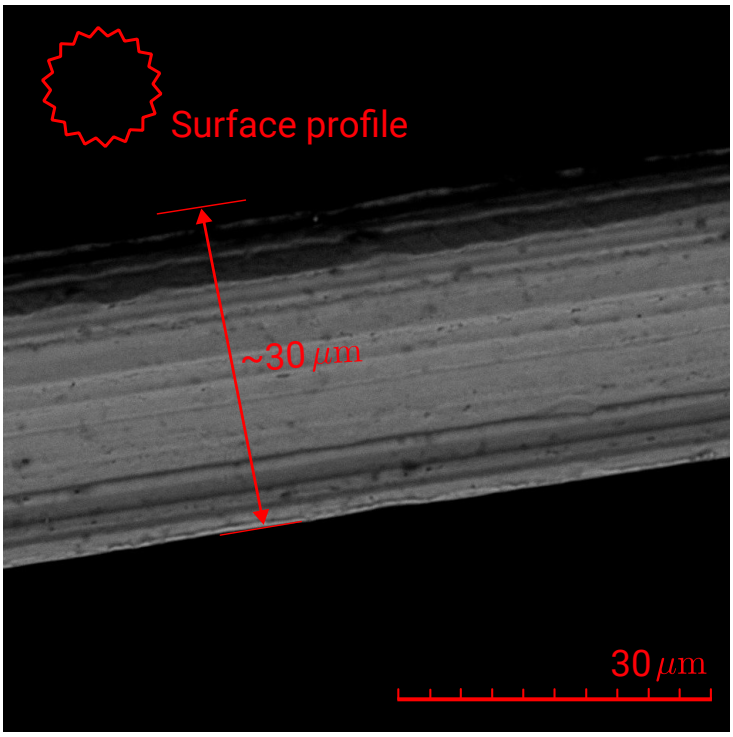

Figure 5.16: SEM image of a new wire.

Figure 5.16 shows the surface detail of a new and unused constantan wire. It is possible to see that the diameter is roughly 30 µm as per specification but the surface profile is not regular. The profile has crests of a size of less than 1 µm which are likely due, because of the regularity, to the manufacturing process. Overall the surface is clean and presents no major damage or contaminant.

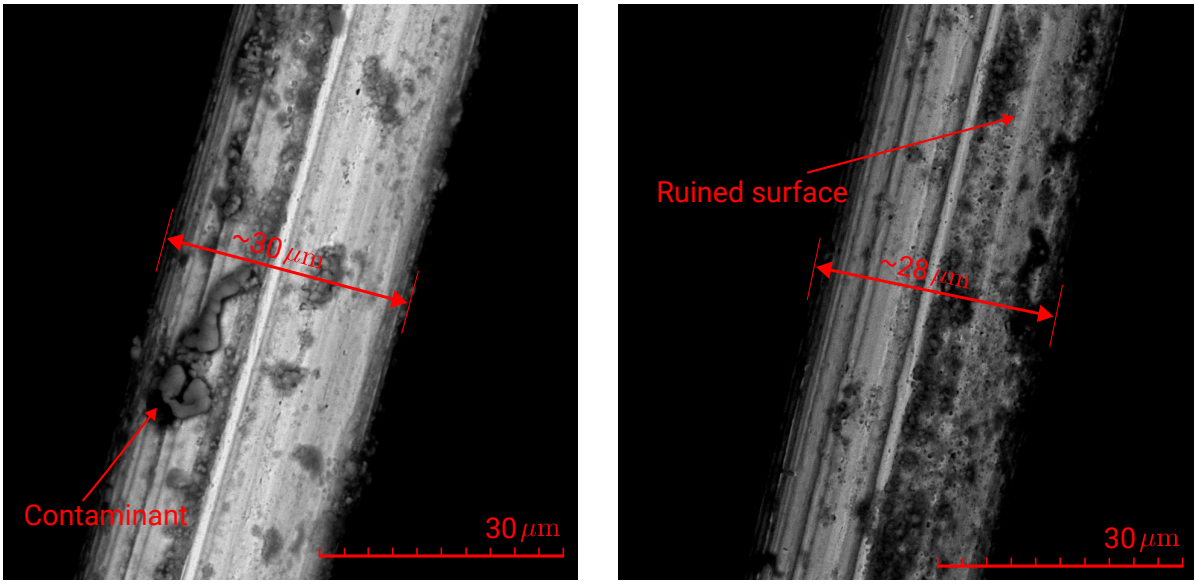

(a) Used Wire (b) Used Wire

Figure 5.17: SEM image of a used wire

Figure 5.17 show the same wire after approximately 1 h of intermittent use (estimation carried out with respect to the number of tests performed with this wire and the mean duration of such tests). This picture was taken after a spurious 5% increase in the current consumption was noticed. In particular, it is hypothesized that Figure 5.17a shows the top of the emitter, i.e. the side which is not facing the collector, and 5.17b shows a side-view (on the right, the side facing the collector and on the left the other side). It is possible to see that the side not facing the collector presents accumulation of contaminants of variable size (1 µm to 30 µm) which are caused by the presence, in the atmosphere, of small particulates which are electrically attracted to the emitter during use. The emitting side shows visible signs of surface damage which result in small irregularities in the surface. It is hypothesized that surface reactions occurring at the emitter are the cause of such damage. The presence of arks and sparks can further damage the emitter rendering the entire wire unusable. This problem is a major concern for any future application of this technology as this level of degradation might not be acceptable in a operating ionic thruster.

6 | Discussion and Conclusion

In this work, a thorough investigation has been conducted to study the effect of various geometrical parameters on the overall performance of the thruster. The experimental setup involved measuring the generated thrust using load cells, in conjunction with recording the electrical data such as current and ignition and working voltages.

The scaling model introduced in this study is a crucial step towards understanding the relationship between the experimental data and the setup conditions. This model involves scaling all the lengths with respect to the gap, and defining dimensionless coefficients for all the physical quantities of interest. With this approach, it is possible to reduce the number of free parameters, making it easier to comprehend the correlations between the different parameters.

The most important discovery made by this study is the fact that the airfoil chord can be significantly decreased from the previous 100 mm value. This can improve the performance since the parasitic drag is minimized but can also make the thruster smaller and the corresponding support structures lighters.

Parameter	New Value	Previous Value	Improvement
Thrust Coefficient	0.40	0.34	17 %
Thrust to Power Coefficient	0.65	0.60	8 %
(Cell) Volumetric Thrust Coefficient	0.10	0.03	230 %

Table 6.1: Comparison between the dimensionless performance indicators of the new C25T6 airfoil and C100T10 airfoil at the standard configuration 1.8

Table 6.1 shows the different dimensionless parameters of the old C100T10 airfoil and the new C25T6 airfoil. It is possible to see that the new configuration optimizes the thrust and the thrust to power by a noticeable amount which shows that the previous configuration developed too much parasitic drag. The biggest increase, however, is seen in the volumetric thrust density coefficient, having used the total cell volume $S(c + d)$.

This result is promising because it opens the possibility to use compact and efficient multi-staged thrusters.

Parameter	Value	SI Unit
Thrust per unit Span	65	mN/m
Thrust to Power	4.4	N/W
(Cell) Volumetric Thrust Density	40	N/m^3

Table 6.2: Dimensional parameters for the C25T6S35 optimized configuration at the standard configuration 1.8

Table 6.2 reports the new performance indicators for the C25T6 optimized configuration. These results have opened the possibility of studying the optimal configurations at different spacings showing that there are two possible optimal configurations that optimize either the thrust density or thrust to power.

(a) Small Spacing Optimal Configuration (b) Large Spacing Optimal Configuration

Figure 6.1: Depiction of the two optimized configuration found by this work

The first configuration, called S10SE, uses C25T2 airfoils, in single emitter configuration, which are thin and can be placed at a 10 mm spacing optimizing the thrust density coefficient whereas the second configuration, called S40DE, uses the same airfoils but in double emitter configuration at a spacing of 40 mm optimizing the thrust to power ratio.

Configuration	C_{TAe}	T/A	C_{TP}	T/P	P/A
S10SE	0.39	$4.42\,N/m^2$	0.55	$3.5\,N/kW$	$1.25\,kW/m^2$
S40DE	0.22	$1.94\,N/m^2$	0.79	$5.06\,N/kW$	$0.38\,kW/m^2$

Table 6.3: Performance indicators for the two optimal configurations found

Table 6.3 reports the performance indicators for the two configurations found. It is possible to see that the S10SE configuration generates a significant amount of thrust per unit area but a large amount of power is required to feed that area whereas the seond configuration generates half of the thrust but requires 3 times less power.

At this point, a general optimization procedure is required in order to choose the correct configuration. This optimization, however, should be performed once the requirements are set which can come in many forms.

The results of this work underscore the need for further investigation in two key areas. First, leveraging these findings, we can identify specific requirements that any future ionic thruster must meet. It is then possible to implement an optimization procedure to fine-tune the thruster's geometric parameters to meet these requirements and optimize its performance.

Secondly, it would be valuable to conduct additional research into the fundamental physics of the thruster. Specifically, it is possible to experimentally test the scaling model with external convection to validate it. Additionally, exploring a range of environmental conditions could simulate different operating environments for the thruster and provide further insights.

Bibliography

[1] M. Belan, L. Arosti, R. Polatti, F. Maggi, S. Fiorini, and F. Sottovia. A parametric study of electrodes geometries for atmospheric electrohydrodynamic propulsion. *Journal of Electrostatics*, 113:103616, 2021.

[2] M. Belan, R. Terenzi, S. Trovato, and D. Usuelli. Effects of the emitters density on the performance of an atmospheric ionic thruster. *Journal of Electrostatics*, 120: 103767, 2022.

[3] B. J. Brelje and J. R. Martins. Electric, hybrid, and turboelectric fixed-wing aircraft: A review of concepts, models, and design approaches. *Progress in Aerospace Sciences*, 2019.

[4] W. Cao, B. C. Mecrow, G. J. Atkinson, J. W. Bennett, and D. J. Atkinson. Overview of electric motor technologies used for more electric aircraft (mea). *IEEE Transactions on Industrial Electronics*, 2012.

[5] C. Charles. Plasmas for spacecraft propulsion. *Journal of Physics D: Applied Physics*, 2009.

[6] F. Chen. *Introduction to Plasma Physics and Controlled Fusion*. Springer International Publishing, 2016.

[7] M. Chirita and A. Ieta. First rotary ionic engine with contra-rotating propellers. *Journal of Propulsion and Power*, pages 1–8, 2022.

[8] A. Fridman and L. Kennedy. *Plasma Physics and Engineering*. Taylor & Francis, 2004.

[9] C. Gilmore and S. Barrett. Electrohydrodynamic thrust density using positive corona-induced ionic winds for in-atmosphere propulsion. *Proceedings of the Royal Society A: Mathematical, Physical and Engineering Sciences*, 471:20140912–20140912, 01 2015.

[10] D. M. Goebel and I. Katz. *Fundamentals of electric propulsion: ion and Hall thrusters*. John Wiley & Sons, 2008.

[11] A. Ieta and M. Chirita. Electrohydrodynamic propeller for in-atmosphere propulsion; rotational device first flight. *Journal of Electrostatics*, 2019.

[12] A. Ieta and M. Chirita. Toroidal counter electrode for ionic propulsion. 2023.

[13] A. Ieta, R. Ellis, D. Citro, M. Chirita, and J. D'Antonio. Characterization of corona wind in a modular electrode configuration. 2013.

[14] J. Jones. A theoretical explanation of the laws of warburg and sigmond. *Proceedings: Mathematical, Physical and Engineering Sciences*, (1960):1033–1052, 1997. ISSN 13645021.

[15] N. Kaptsov. *Elektricheskie yavleniya v gazakh i vakuume*. 1947.

[16] V. Khomich and I. Rebrov. In-atmosphere electrohydrodynamic propulsion aircraft with wireless supply onboard. *Journal of Electrostatics*, 2018.

[17] V. Khomich, V. Malanichev, and I. Rebrov. Electrohydrodynamic thruster for near-space applications. *Acta Astronautica*, 180:141–148, 2021.

[18] H. Kramers. Heat transfer from spheres to flowing media. *Physica*, 1946.

[19] E. Kuffel, W. Zaengl, and J. Kuffel. Chapter 5 - electrical breakdown in gases. In E. Kuffel, W. Zaengl, and J. Kuffel, editors, *High Voltage Engineering Fundamentals (Second Edition)*, pages 281–366. Newnes, Oxford, second edition edition, 2000. ISBN 978-0-7506-3634-6. doi: https://doi.org/10.1016/B978-075063634-6/50006-X. URL `https://www.sciencedirect.com/science/article/pii/B978075063634650006X`.

[20] E. B. Kulumbaev, V. M. Lelevkin, I. A. Niyazaliev, and A. V. Tokarev. Characteristics of a corona discharge with a hot corona electrode. 2011.

[21] J. Lemetayer, C. Marion, D. Fabre, and F. Plouraboué. Multi-inception patterns of emitter array/collector systems in dc corona discharge. *Journal of Physics D: Applied Physics*, 55, 2022.

[22] K. Masuyama and S. Barrett. On the performance of electrohydrodynamic propulsion. *Royal Society of London Proceedings Series A*, 469:20623–, 2013.

[23] S. Mazouffre. Electric propulsion for satellites and spacecraft: Established technologies and novel approaches. *Plasma Sources Science and Technology*, 2016.

[24] N. Monrolin, F. Plouraboué, and O. Praud. Electrohydrodynamic thrust for in-atmosphere propulsion. *AIAA Journal*, 55:4296–4305, 2017.

[25] E. Moreau, N. Benard, J.-D. Lan-Sun-Luk, and J.-P. Chabriat. Electrohydrodynamic force produced by a wire-to-cylinder dc corona discharge in air at atmospheric pressure. *Journal of Physics D: Applied Physics*, 46(47):475204, 2013.

[26] N. Mott and R. Gurney. *Electronic Processes in Ionic Crystals*. The International series of monographs on physics. Clarendon Press, 1957.

[27] F. Peek. *Dielectric Phenomena in High Voltage Engineering*. McGraw-Hill Book Company, Incorporated, 1920.

[28] J. S. Townsend. *Electricity in gases*. Oxford Press, 1914.

[29] R. Vaddi, Y. Guan, A. Mamishev, and I. Novosselov. Analytical model for electrohydrodynamic thrust. *Proceedings of the Royal Society A*, 476, 2020.

[30] N. Vega, H. Xu, J. Abel, and S. Barrett. Performance of decoupled electroaerodynamic thrusters. *Applied Physics Letters*, 118, 2021.

[31] J. Wilson, H. Perkins, and W. Thompson. An investigation of ionic wind propulsion. 2009.

[32] H. Xu, Y. He, K. Strobel, C. Gilmore, S. Kelley, C. Hennick, T. Sebastian, M. Woolston, D. Perreault, and S. Barrett. Flight of an aeroplane with solid-state propulsion. *Nature*, 563, 11 2018.

A | Voltage Behaviour of different airfoils

This chapter provides an analysis of the voltage dependence of performance indicators for different airfoils in the parameter space, which was conducted in parallel with the evaluation presented in Section 5.2. The purpose of these studies was two-fold: first, to gain diagnostic insights into the performance of the airfoils, and second, to validate the results obtained from the parameter space evaluation and the dimensionless model. By examining the agreement of the full voltage curve with the considerations given in Section 5.2, this chapter is able to provide further validation for the findings.

A.1. C100 airfoils

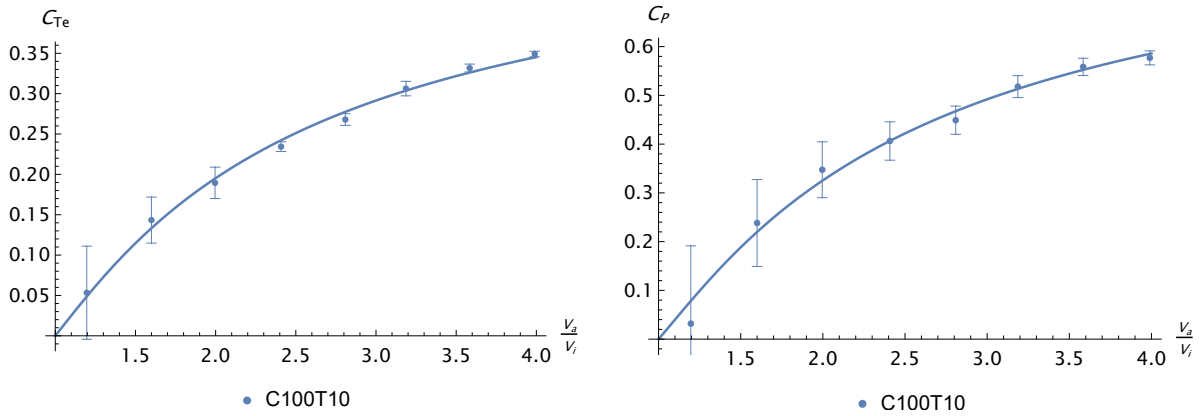

(a) Thrust Coefficient

(b) Power Coefficient

Figure A.1: Voltage dependence of the thrust and thrust to power coefficient of the C100 airfoils

A.2. C40 airfoils

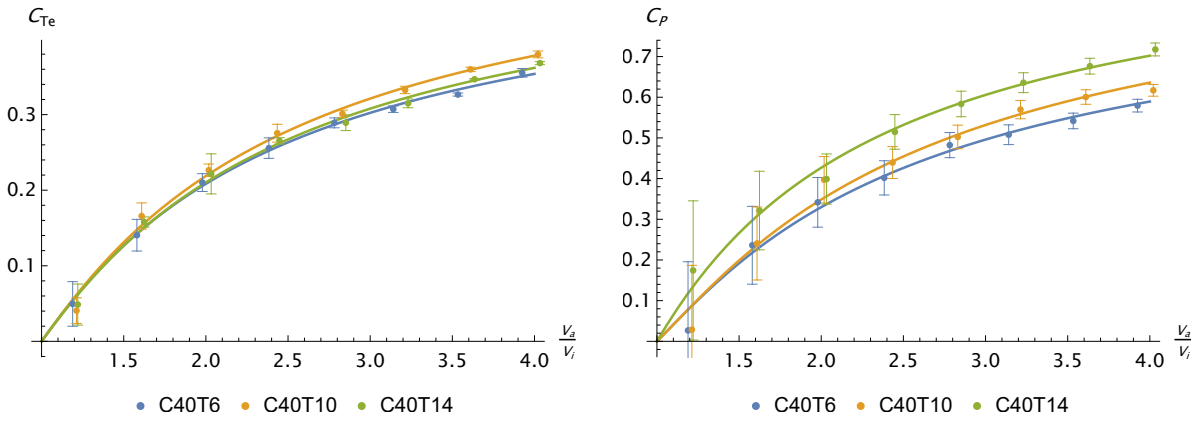

(a) Thrust Coefficient (b) Power Coefficient

Figure A.2: Voltage dependence of the thrust and thrust to power coefficient of the C40 airfoils

A.3. C25 airfoils

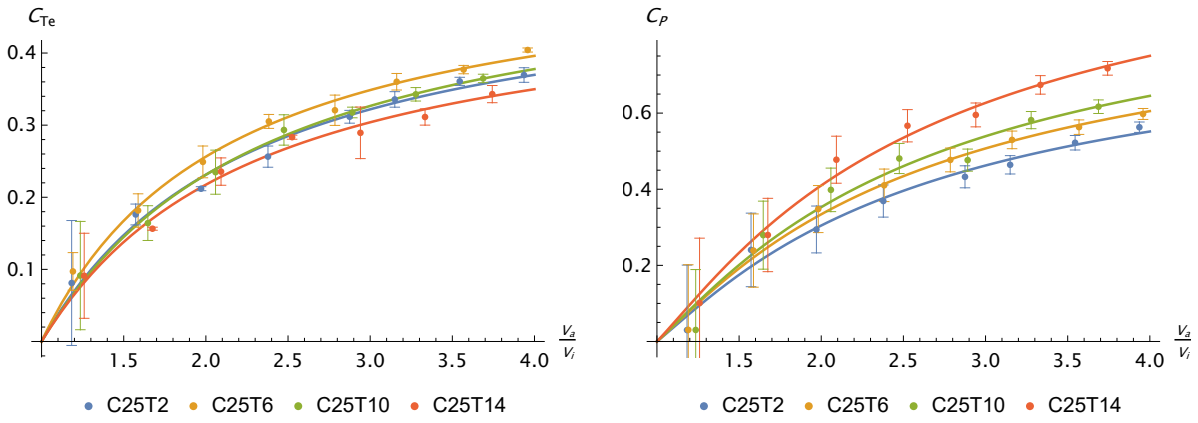

(a) Thrust Coefficient (b) Power Coefficient

Figure A.3: Voltage dependence of the thrust and thrust to power coefficient of the C25 airfoils

A.4. C15 airfoils

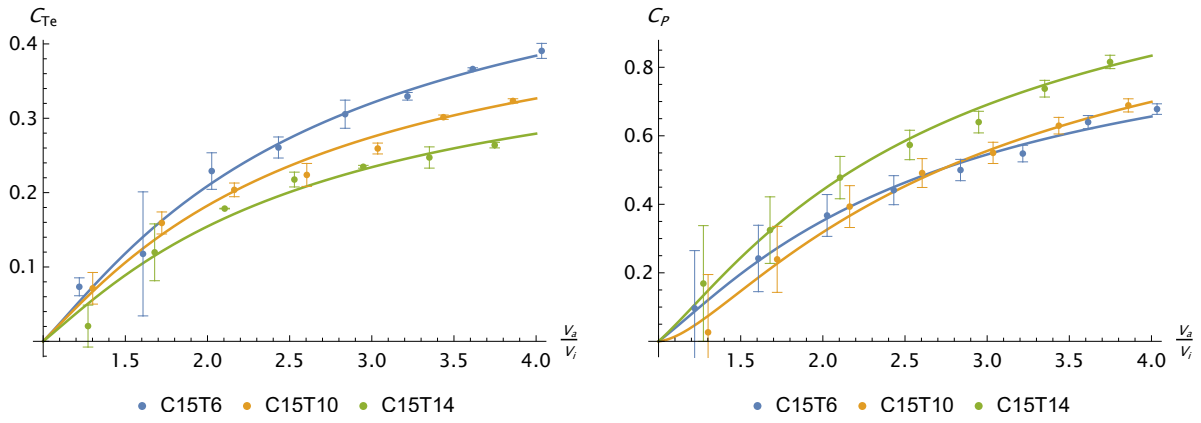

(a) Thrust Coefficient

(b) Power Coefficient

Figure A.4: Voltage dependence of the thrust and thrust to power coefficient of the C15 airfoils

B | Hot Wire Emitters

This appendix is devoted to the study of the effect of the emitter temperature to improve the efficiency of ionic thrusters.

Kulumbae et al. [20], performed a similar study and found that increasing the emitter temperature has the positive effect of reducing the ignition voltage. This is due to the fact that increasing the emitter temperature does not affect the drift region properties (such as mobility, density, ...) as long as the power transferred to the air is small. For this reason, increasing the temperature can facilitate the ionization of the gas and hence decrease the temperature [20].

Recalling Peek's formula for the inception field (explained in 2.32), it is possible to compute an estimation of the ignition voltage solving Poisson's equation in an axial-symmetric configuration

$$V_i = E_b\delta(1 + \frac{k_1}{\sqrt{\delta r_e}})r_e \ln\left(\frac{\mathrm{d}}{\mathrm{r_e}}\right) \tag{B.1}$$

Changing the temperature will affect δ which is the gas number density ratio. Using the ideal gas law, $P = n\mathrm{k_B}\mathrm{T}$ it is possible to see that the gas number density decreases linearly with the temperature. The effect on the ignition voltage is therefore, calling $\alpha = \frac{k_1}{\sqrt{r_e}}$,

$$\frac{V_{\mathrm{i,HOT}}}{V_{\mathrm{i,COLD}}} = \frac{\delta + \alpha\sqrt{\delta}}{1 + \alpha} \ . \tag{B.2}$$

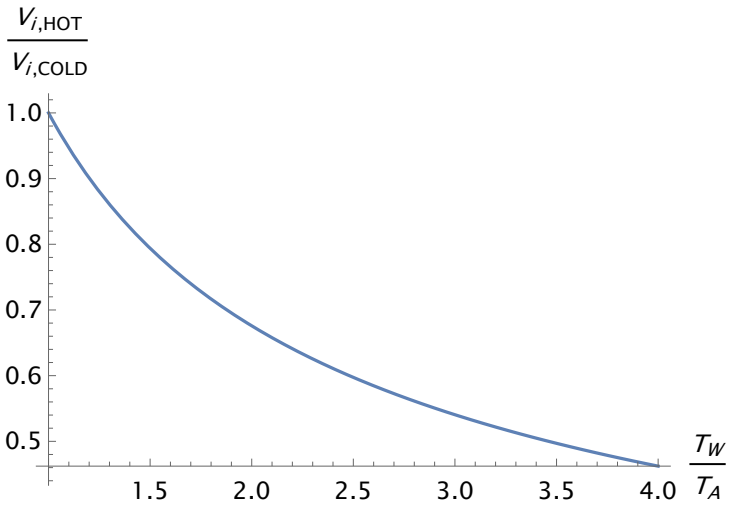

Figure B.1: Effect of the wire temperature on the inception voltage.

Figure B.1 shows that increasing the wire temperature has a huge effect on the inception voltage as increasing the wire temperature to up to 300 K (3 times the ambient temperature, T_A) can decrease the inception voltage by more than 60 %. This model, although simple, has been validated by [20] with temperature up to 700 K and showed that deviations from this trend are within 5 %.

This can potentially have a huge impact on the performance of EHD thrusters for two main reasons. First and foremost decreasing the inception voltage means that, in order to maintain the same dimensionless voltage $\hat{V}$, the applied voltage can be decreased. This will negatively impact the thrust since the reference value depends on V_a^2 but greatly improve the thrust to power ratio. It is in fact true that if the applied voltage is reduced to a factor of 60 % the thrust to power ratio will experience a relative increase of 60 %. This can boost the performance of configurations that have a low thrust to power ratio. Moreover; this decrease in the inception voltage can limit, or even eliminate the shielding effect making the thruster able to fly in multiple emitter configurations or at very low spacings. However, it is also true that the power required to heat the wire must be accounted for in the general power consumption balance.

The general power balance equation for the heated wire, per unit length, reads

$$R_w I_w^2 = c_w h (T_w - T_a) \tag{B.3}$$

Where $R_w = R_a(1 - \alpha_T(T_w - T_a))$ is the wire resistance at a temperature T_w, I_w is the current flowing in the wire, $c_w = 2\pi r_e$ its circumference and h the heat transfer coefficient.

In particular, $h = \frac{\mathrm{Nu}\ \mathrm{k}}{2\ r_e}$ where Nu is the Nusselt number and k the air thermal conductivity. It was estimated that the ratio between the wire Reynolds number, computed using the reference velocity at 20 kV, and the square of the Grashof number is small, around 10^{-4}, at 1000 K, indicating that forced convection prevails over natural convection. For this reason, the following empirical correlation was used to compute the Nusselt number

$$\mathrm{Nu} = 0.39 + 0.51\sqrt{\mathrm{Re}}\ . \tag{B.4}$$

This formula is due to Kramers [18] and is valid for a Reynolds number (computed using the incoming flow temperature) between 2.5 and 1500 (in our case the emitter Reynolds number is 5).

Using this correlation, the balance equation can be solved to find the current and power consumption of the hot wire.

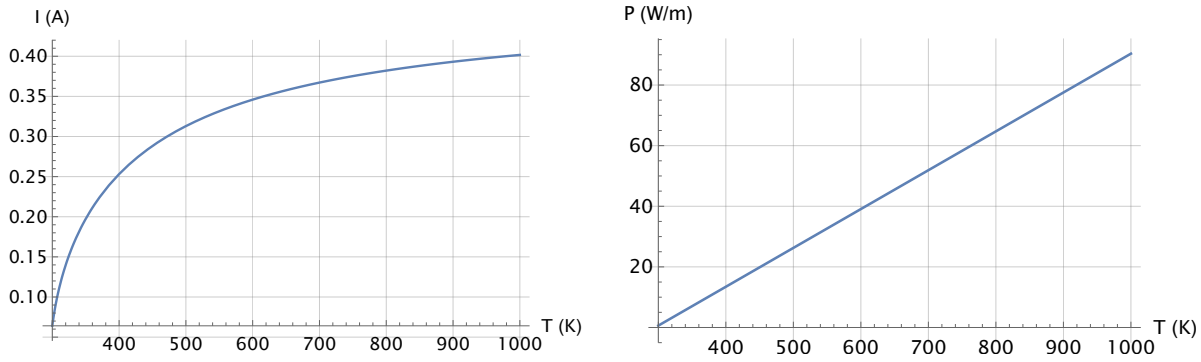

(a) Current Consumption

(b) Power Consumption

Figure B.2: Current and power consumption of a hot wire

Figure B.2 shows that the current consumption, for a 30 µm platinum wire, is very high and it gets worse as the wire diameter is increased (because more power is required to keep the wire temperature).

B.1. Performance Computation

As mentioned in previous sections, a possible improvement is due to the fact that increasing the temperature will decrease the inception voltage hence the thruster will require a smaller voltage to operate in the same condition. Using the fact that the C25T6 in the standard configuration, reported in 1.8, has a C_{Te} of 0.4 and a C_P of 0.5 at $\hat{V} = 4$ the

total power, per unit length, required to drive the thruster will be the sum of the corona power and the hot wire power

$$P = \mu_q \epsilon_0 \frac{V_a^3}{d^2} 0.5 + R_w I_w^2 \ . \tag{B.5}$$

The applied voltage required to drive the thruster at $\hat{V} = 4$ will be $V_a = 4V_i$ hence increasing the temperature can potentially have a beneficial effect.

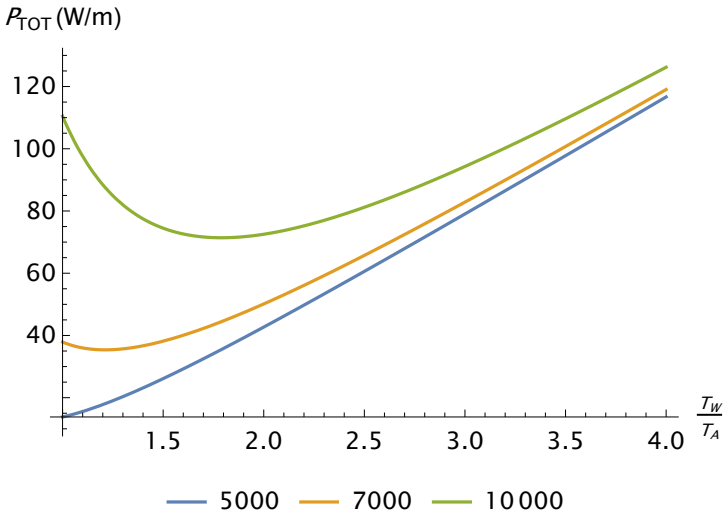

Figure B.3: Effect of the wire temperature on the total power consumption for different values of the inception voltage.

Figure B.3 shows that the functional dependence of the total power consumption admits a minimum at a high temperature only if the inception voltage is high. In the case of the standard configuration the inception voltage is 5 kV so no improvement is possible.

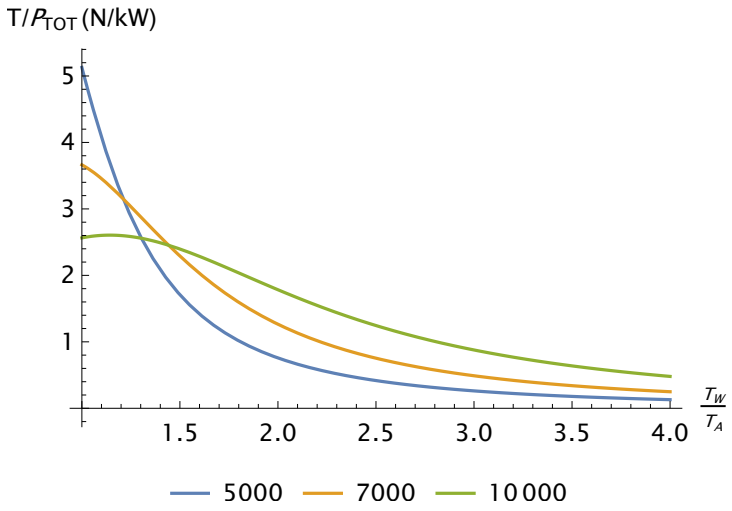

Figure B.4: Effect of the wire temperature on the total thrust to power consumption for different values of the inception voltage.

The Thrust to Power being defined as the ratio of the thrust and the total power consumption will also show the effect of the reduced thrust. Figure B.4 shows that the improvements, even assuming a large inception voltage are negligible.

Overall, increasing the wire temperature does not have a beneficial effect on the performance apart for very power demanding configurations that require a high voltage. The benefits of using a hot emitter in configurations where the thruster has a very high inception voltage still needs to be evaluated because the improvement on the dimensionless coefficients strongly depends on the working $\hat{V}$ point. Even in this case, the wire diameter would have to be very small to limit the power consumption which might not be feasible for robustness requirements.

List of Figures

List of Tables

List of Symbols

Variable	Description	SI unit
$\boldsymbol{u}$	Neutral Gas Velocity	m/s
$\boldsymbol{v}$	Ion Velocity	m/s
n	Number Density	$1/\mathrm{m}^3$
m	Mass	kg
q	Charge	C
ν^{coll}	Collision Frequency	1/s
P	Pressure	N/m^2
$\boldsymbol{E}$	Electric Field	V/m
ρ	Neutral Gas Mass Density	kg/m^3
ρ_q	Charge Density	C/m^3
μ_q	Ion Mobility	$\mathrm{m}^2/\mathrm{s\ V}$
μ	Air Dynamic Viscosity	Pa/s
ν	Air Kinematic Viscosity	m^2/s
V	Voltage	V
T	Temperature	K
k_B	Boltzmann Constant	$\mathrm{m}^2\ \mathrm{kg}/\mathrm{s}^2\ \mathrm{K}$
ϵ_0	Dielectric Vacuum Permittivity	F/m
α	Townsend's First Coefficient	1/m
η	Townsend's Reattachment Coefficient	1/m
γ	Townsend's Second Coefficient	–
δ	Gas Number Density Ratio	–
R	Resistance	Ω

Physical Parameters

Variable	Description	SI unit
t	Collector Thickness	m
c	Collector Chord	m
S	Electrode Spacing	m
d	Electrode Gap	m
r_e	Emitter Radius	m
a	Ground Strip x-Axis Length	m
b	Span	m

Geometrical Parameters

Variable	Description	SI unit
T	Thrust	N
P	Electrical Power Consumption	W
T/P	Thrust to Power	N/W
T/A	Surface Thrust Density	N/m^2
T/Al	Volumetric Thrust Density	N/m^3
P_u	Mechanical Power	W

Performance Indicators

Variable	Description
C_T	Thrust Coefficient
C_P	Electrical Power Coefficient
C_{TP}	Thrust to Power Coefficient
C_{TA}	Surface Thrust Density Coefficient
C_{TV}	Volumetric Thrust Density Coefficient
C_{Pu}	Mechanical Power Coefficient
η	Mechanical Efficiency

Dimensionless Coefficients

Ringraziamenti

Scrivere questi ringraziamenti è stata una delle cose più difficili che abbia mai fatto, poiché le persone che mi hanno accompagnato durante questi 24 anni sono state tutte speciali e mi hanno dato un contributo importante nella mia vita. Sono davvero grato per aver avuto la fortuna di avere famiglia e amici così meravigliosi al mio fianco, che mi hanno sostenuto e aiutato a diventare la persona che sono oggi.

Innanzitutto, voglio ringraziare il professor Belan per essere stato al mio fianco in tutto il percorso di tesi e per aver condiviso con me la sua passione per la ricerca e la sperimentazione. Desidero inoltre ringraziare Antonio e tutto il personale tecnico-amministrativo del DAER per l'aiuto e il supporto forniti durante il lavoro. Grazie anche a tutti i docenti che ho avuto a scuola, a Padova e al Poli. Grazie per essere riusciti a trasmettermi la passione per la scienza e l'aerodinamica.

Un ringraziamento speciale va ai miei compagni di laboratorio: Domenico, Jacopo, Mattia, Guido e Mirko. Condividere con loro i momenti felici e difficili di questo percorso è stato davvero un'esperienza indimenticabile. Grazie per il supporto reciproco e per essermi stati accanto in ogni occasione.

Non riesco a esprimere a parole la gratitudine che provo verso la mia famiglia, in particolare verso Mamma, Papà, Frank, Ivan, Giulio, Maria e Armando. Il loro amore e sostegno in tutti questi anni è stato inestimabile, e non ci sono parole per quantificare quanto io apprezzi la loro presenza nella mia vita. Siete stati la mia roccia, il mio motore e la mia ispirazione in ogni momento, e ogni mio successo è il risultato del vostro incoraggiamento e della vostra fiducia in me. Vi voglio un mondo di bene. Desidero anche ringraziare nonno Italo e nonna Giulia, che ci hanno lasciato di recente. Sono stati i primi a trasmettermi la passione per la scienza e la cultura, plasmandomi con pazienza e affetto.

Ringrazio i miei amici più cari, le persone con cui sono cresciuto a Budoia. Conosco molti di voi dalle scuole materne e non ci siamo mai persi di vista. Insieme abbiamo attraversato momenti di gioia e di difficoltà, affrontato le prime sfide e raggiunto i primi grandi traguardi. Mi sento fortunato ad avere il privilegio di chiamarvi amici e sono

orgoglioso di conoscervi. Non so quale futuro ci riserverà la vita, ma sappiate che avrete sempre un posto speciale nel mio cuore, come una seconda famiglia. Vorrei ringraziare di cuore Andrea, Daniele, Riccardo, Luca, Ani, Arci, Polly, Elisabetta, Annamaria, Jacopo, Giovanni, Nina, Andrei, Edgar, Davide, Tramo, Micaela e Anna per la loro preziosa amicizia.

Desidero ringraziare di cuore anche i miei compagni di triennale, gli *Umpa Lumpa della Scienza*. Quando sono arrivato a Padova, mi sentivo spaventato e fuori luogo in questo nuovo ambiente così diverso dalla mia Budoia. Tuttavia, voi mi avete accolto come un amico, accettandomi per quello che sono, pregi e difetti compresi. Sorrido mentre ricordo tutti i momenti che abbiamo condiviso insieme, dalle prime feste nel mio appartamento dopo lunghe giornate di studio, alle corse per prendere i posti in terza fila alle 7.30 del mattino, fino ai mesi difficili della pandemia, durante i quali abbiamo festeggiato le nostre lauree. Vorrei mettere in loop gli anni dai 19 ai 21 per rivivere ancora una volta questi momenti. Grazie per essere stati parte della mia vita e per avermi regalato ricordi che custodirò per sempre nel mio cuore. Grazie Jack, Alessandra, Carmen, Franci, Giorgia, Leo, Alessandro, Fabio, Gian e Andrea.

Desidero esprimere la mia gratitudine agli amici che ho incontrato al Politecnico di Milano. Quando sono arrivato a Milano, mi sono trovato solo e ho dovuto iniziare da zero. Questa situazione è stata resa ancora più difficile dalla pandemia, che ha segnato profondamente le nostre vite. Incontrarvi è stata la cosa più bella che mi sia capitata al Poli. Ricordo come ci siamo sostenuti a vicenda durante il primo semestre, colpiti dalla seconda ondata della pandemia. Ricordo le feste del venerdì sera al BL27, in cui cantavamo e bevavamo, e le nottate passate a festeggiare in piazza Leo. Ricordo quanto abbiamo sofferto durante il terzo semestre, pieno di progetti e cose da fare. In questi anni abbiamo stretto un forte legame, che porterò con me per sempre. Grazie soprattutto a Riccardo, Erik, Carlo, Lorenzo, Leonardo, Sergio e Federico voi siete state le prime persone che ho conosciuto al Poli. Grazie ai fioi di Bovisa: Enrico, Adi, Martina, Anthony, Aki, Mattia e Lorenzo con cui ho passato fin troppi bei momenti e 1000 storie da raccontare. Grazie a Marta, Franci, Cosimo e Reda, *the crazy people of CFD*, avete reso i noiosi progetti dei corsi una meravigliosa avventura. Grazie Pier, Azzurra e Edo, i ragazzi di piazza Leo, grazie per le serate passate tra birra, carbonara e coprifuoco. Grazie ai ragazzi dei *Poli-Friday* (siete davvero tanti) per i venerdì sera al BL27 e dintorni. Grazie Daniele, Matteo, Luca e Ludo per le tante serate passate assieme e il sostegno all'uni. Grazie, grazie davvero.

Sicuramente, il mio più grande merito è stato conoscervi e poter far parte delle vostre vite.